Gas Turbine Laboratory
Department of Aeronautics and Astronautics
Massachusetts Institute of Technology
Cambridge, MA 02139

A Final Technical Report

FA9550-05-1-0050

entitled

PERFORMANCE LIMITING FLOW PROCESSES IN HIGH-STATE LOADING HIGH-MACH NUMBER COMPRESSORS

submitted to

Ms. Laura Cooney
AFOSR/NA
875 North Randolph Street
Suite 325, Room 3112
Arlington, VA 22203

Lt. Col Rhett Jefferies
Technical Program Monitor

PRINCIPAL INVESTIGATOR: Dr. Choon S. Tan
Senior Research Engineer
Gas Turbine Laboratory
Tel: 617-253-7524; FAX: 617-258-6093
email: choon@mit.edu

PERIOD OF INVESTIGATION: December 15, 2004 - December 14, 2007

March 13, 2008

20080527154

REPORT DOCUMENTATION PAGE

Form Approved
OMB No. 0704-0188

Public reporting burden for this collection of information is estimated to average 1 hour per response, including the time for reviewing instructions, searching existing data sources, gathering and maintaining the data needed, and completing and reviewing this collection of information. Send comments regarding this burden estimate or any other aspect of this collection of information, including suggestions for reducing this burden to Department of Defense, Washington Headquarters Services, Directorate for Information Operations and Reports (0704-0188), 1215 Jefferson Davis Highway, Suite 1204, Arlington, VA 22202-4302. Respondents should be aware that notwithstanding any other provision of law, no person shall be subject to any penalty for failing to comply with a collection of information if it does not display a currently valid OMB control number.
PLEASE DO NOT RETURN YOUR FORM TO THE ABOVE ADDRESS.

1. REPORT DATE *(DD-MM-YYYY)*	2. REPORT TYPE	3. DATES COVERED *(From - To)*
03-13-08	Final Technical Report	12-15-04 to 12-14-08

4. TITLE AND SUBTITLE
Performance Limiting Flow Processes in High-State Loading High-Mach Number Compressors

5a. CONTRACT NUMBER

5b. GRANT NUMBER
FA9550-05-1-0050

5c. PROGRAM ELEMENT NUMBER

6. AUTHOR(S)
Tan, Choon S. (Dr.)

5d. PROJECT NUMBER

5e. TASK NUMBER

5f. WORK UNIT NUMBER

7. PERFORMING ORGANIZATION NAME(S) AND ADDRESS(ES)

Massachusetts Institute of Technology
Gas Turbine Laboratory
Bldg 31 Rm 267
77 Massachusetts Avenue
Cambridge, MA 02139

8. PERFORMING ORGANIZATION REPORT NUMBER
n/a

9. SPONSORING / MONITORING AGENCY NAME(S) AND ADDRESS(ES)
Air Force Aerospace Research-OSR
AFOSR/PKC/NA
875 North Randolph Street
Room 3112
Arlington, VA 22203-1954

10. SPONSOR/MONITOR'S ACRONYM(S)
n/a

11. SPONSOR/MONITOR'S REPORT NUMBER(S)

12. DISTRIBUTION / AVAILABILITY STATEMENT
unlimited - Distribution A

AFRL-SR-AR-TR-08-0288

13. SUPPLEMENTARY NOTES
n/a

14. ABSTRACT In high-stage loading high-Mach number (HLHM) compressors, counter-rotating pairs of discrete vortices are shed at the trailing edge of the upstream blade row at a frequency corresponding to the downstream rotor blade passing frequency. This is a consequence of an alternating change in blade loading caused by the passage of shocks or compression waves emanating from the downstream rotor. While this effect is present at any Mach number the combination of high loading and high Mach number mean that the attenuation of the rotor pressure field with upstream distance is much less than at either lower loading or subsonic Mach numbers, i.e., the upstream extent of rotor influence is a generic feature for HLHM compressors. Computations and physical arguments have shown that the pitchwise location at which these discrete vorticies enter the rotor passage has a substantial impact on the rotor performance, for example work input and entropy (loss) generation. The features of the effect have been characterized by a reduced frequency parameter defined as the ratio of convective time for the vortex to travel from trailing edge of the upstream blade-row to the leading edge of downstream rotor to vortex shedding time (rotor blade passing time). Thus a change in inter-blade-row spacing, rotor wheel speed, through-flow velocity in the intra-stator/vane-rotor gap, rotor pitch, and shock angle would result in rotor performance change. The flow in a two-dimensional diffuser subjected to a wake and jet is used to provide a physical context explaining the response of the rotor performance to the discrete wakes. This provides a more direct avenue for establishing the scaling of rotor performance change, appropriately non-dimensionalized, in terms of the reduced frequency, Mach number and characteristics of discrete vorticies (i.e. its strength and size).

15. SUBJECT TERMS
High-stage loading High Mach number compressor, Unsteady blade-row interactions

16. SECURITY CLASSIFICATION OF:			17. LIMITATION OF ABSTRACT	18. NUMBER OF PAGES	19a. NAME OF RESPONSIBLE PERSON
a. REPORT	b. ABSTRACT	c. THIS PAGE			Dr. Choon S. Tan
unlimited	unlimited	unlimited	none	63	19b. TELEPHONE NUMBER *(include area code)* 617-253-7524

CONTENTS

	Nomenclature	i
1.0	Summary	1
1.1	Introduction and Objectives	1
1.2	Research Abstract	1
2.0	New Findings and Accomplishments	2
3.0	Technical Background	3
4.0	Research Questions and Technical Approach	6
4.1	Numerical Tool	8
4.2	HLHM Compressor Stage: AFRL Stage Matching Investigation Compressor	10
4.3	Overall Summary of Approach	13
5.0	Quantification of Sources for Entropy Generation	15
5.1	Sources of Entropy Generation	16
5.2	Computation of Local Dissipation	19
5.3	Procedure to Compute Shock Entropy Rise	21
6.0	Vortex Trajectory Within the Rotor	25
6.1	Parametric Dependence of Vortex Trajectory within Rotor	26
6.2	Vortex Trajectories in the Unsteady Two-dimensional Computations	27
6.3	Vortex Strength and Size in Vane-Rotor Gap Region	30
6.4	Rotor Response to a Change in Vortex Trajectory	33
6.5	Results of Zachcial and Nurnberger	37
6.6	A Summary on Impact of Vortex Trajectory on Rotor Performance	38
7.0	Flow Modeling on Effect of Vortex Trajectory within Rotor	38
7.1	Rotor Response to Pitchwise Shift in Inlet Total Pressure Non-uniformity	39
7.2	Analogy with Diffuser Response to Wake and Jet Inlet Velocity Profile	43
7.3	Scaling of Effect Associated with IGV-Rotor Interactions	45
8.0	Estimating Rotor Performance Change in Three-dimensional Flow	48
9.0	Overall Summary and Conclusions	51
10.0	References	53
11.0	Appendices	55
12.0	Personnel Supported	61
13.0	Publications	61
14.0	Theses	61
15.0	Honors and Awards	61
16.0	Transitions	61
17.0	AFRL Points of Contact	62
18.0	AFRL-MIT Collaboration	62

Nomenclature

Symbols

A	area
C_p	pressure rise coefficient
c_x	axial rotor chord length
k	thermal conductivity
L	axial gap spacing
M_{rel}	relative Mach number
$\dot{m}$	mass flow rate
$nblades$	number of rotor blades
p	pressure
p_t	stagnation pressure
R	ideal gas constant
r	radius
$\bar{r}^{\omega}$	vorticity-weighted radius
s	entropy
T	temperature
T_t	stagnation temperature
TR	stagnation temperature ratio
t	time
U	mean axial velocity
u	velocity or axial velocity component
v	tangential velocity component
W	blade pitch
x	axial direction
y	tangential or pitch-wise direction
α	Flow angle
δ^*	displacement thickness
ϕ	shock angle
Γ	circulation

γ	ratio of specific heats
η	adiabatic efficiency
λ	trailing edge blockage
θ	momentum thickness
θ^*	energy thickness
ρ	density
τ_{ij}	stress tensor
τ	time period
Ω	rotor rotational speed
ω	vorticity

Subscripts

E	free stream condition
ref	reference conditions
1	blade-row inlet
2	blade-row exit
2D	two-dimensional geometry
θ	Tangential component

1.0 Summary

1.1 Introduction and Objectives

This document constitutes the final report on a research program on "Performance Limiting Flow Processes In High-Stage Loading High-Mach Number Compressors"

The objectives of the research program are:

(1) to determine the impact, on efficiency and peak pressure rise potential, of flow processes in high-stage loading, high Mach number (HLHM) compressor stages.

(2) to quantify the conditions at which the above processes of entropy and flow blockage generation lead to a marked increase in sensitivity to geometrical and operational changes.

Two specific flow processes are of interest for the flow regimes encountered in HLHM compressor stages. One is the interaction between shear layers from one blade row and the shock systems from a downstream blade row. The second is the enhanced influence of unsteadiness, from adjacent blade rows on leakage flow at rotor or stator end gaps. Thus the phenomena which need to be examined are not only local to a given blade row (and can thus be viewed in a steady manner) but also depend on the coupling between blade rows in an inherently unsteady manner. It is also suggested that for the flow regimes unique to HLHM compressors the effects associated with these flow processes interact strongly enough that they cannot be superposed

1.2 Research Abstracts

In high-stage loading high-Mach number compressors, counter-rotating pairs of discrete vortices are shed at the trailing edge of the upstream blade row at a frequency corresponding to the downstream rotor blade passing frequency. This is a consequence of an alternating change in blade loading caused by the passage of shocks or compression waves emanating from the downstream rotor. While this effect is present at any Mach number the combination of high loading and high Mach number mean that the attenuation of the rotor pressure field with upstream distance is much less than at either lower loading or subsonic Mach numbers, i.e., the upstream extent of rotor influence is a generic feature for HLHM compressors. Computations and physical arguments have shown that the pitchwise location at which these discrete vortices enter the rotor passage has a substantial impact on the rotor performance, for example work input and entropy (loss) generation. The features of the effect have been characterized by a reduced frequency parameter defined as the ratio of convective time for the vortex to travel from trailing edge of the upstream blade-row to the leading edge of downstream rotor to vortex shedding time (rotor blade passing time). Thus a change in inter-blade-row spacing, rotor wheel speed, through-flow velocity in the intra-stator/vane-rotor gap, rotor pitch, and shock angle would result in rotor performance change. The flow in a two-dimensional diffuser subjected to a wake and jet is used to provide a physical context explaining the response of the rotor performance to the discrete wakes. This provides a more direct

avenue for establishing the scaling of rotor performance change, appropriately non-dimensionalized, in terms of the reduced frequency, Mach number, and characteristics of discrete vortices (i.e. its strength and size).

2.0 New Findings And Accomplishments

The new findings and accomplishments are delineated in the following:

- A general framework and computational methodology is developed for quantifying local entropy generation in transonic compressors, even in regions with high spatial gradients, such as shock waves.

- In HLHM a new mechanism, involving the generation of a pair of counter-rotating vortices at upstream stator blade trailing by downstream rotor compression wave system and their interaction, has been identified and quantified for its impact on performance.

- The impact of vortex trajectory within the rotor passage on rotor efficiency, pressure rise and work input is determined. A non-dimensional parameter, the reduced frequency parameter, to characterize the trajectory of the vortices is defined. The reduced frequency is the ratio between the convective time scale for the vortices to travel the length of the axial gap between the vane and rotor blade rows, and the rotor period.

- The time-average response of the rotor performance to the discrete wakes can be usefully explained in terms of the flow in a two-dimensional diffuser subjected to a wake and jet.

- A scaling for the time-average response of the rotor performance in terms of the reduced frequency, Mach number, and characteristics of discrete vortices (i.e. its strength and size) is established.

- A flow model is developed for estimating the change in rotor performance with intra-blade row spacing for HLHM compressor stage.

Besides the scientific findings and accomplishments delineated above, the research has fostered a successful collaboration between the Compressor Aerodynamics Research Laboratory of Air Force Research Laboratory and the MIT Gas Turbine Laboratory. The collaboration consisted of: (i) regular semi-weekly teleconference which includes sharing of ideas and interpretation of computed results as well as useful suggestions on the research; (ii) AFRL providing computational resources and experimental information; and (iii) a member of the CARL research team serving on the Doctoral Thesis Committee of the doctoral student.

3.0 Technical Background

A strong incentive exists to reduce airfoil count in aircraft engine core compressors. One driver for this is the desire for affordability (the first A in the Air Force acronym VAATE – Versatile, Affordable, and Advanced Turbine Engine). A basic constraint on blade reduction is seen from the Euler turbine equation, which shows that, although a design can be carried out in different ways to obtain increased stagnation enthalpy rise, and hence pressure ratio, with fewer blades or fewer blade rows, one must increase blade loading and/or wheel speed. For the largest impact both loading and wheel speed must increase, with the consequence that the regime of operation consists of highly loaded blades at transonic Mach numbers. In this regime, however, substantial difficulties have been encountered in obtaining efficient performance at design, let alone the additional constraints of doing this with compressed development time.

A further dimension to the problem is that it is essential to not only obtain appropriate design point efficiency but also to *retain* this efficiency in response to geometric and operational variability. Put another way, the machine should have a gradual fall-off in performance with changes from the nominal geometry (from wear as well as from manufacturing variability), rather than a sharp drop-off. This is difficult to achieve at conditions of high loading and high Mach number. Addressing the fluid dynamic difficulties of these highly loaded, high Mach number[1] (HLHM) compressor stages is a key aspect described in this report.

The above is a very broad statement and we need to state with more precision what is meant. At one level, some of the key technical issues in designing blading for such stages may be viewed as well known. For example textbooks on compressors (Cumpsty, 1989) show narrowing of the incidence range for low loss operation as the Mach number increases. The sensitivity of the flow conditions in a channel-to-channel area ratio when the Mach number is near unity is also understood. These are severe constraints which characterize the regime of interest.

To put this in another way, from basically one-dimensional (or meanline) descriptions, one can see high sensitivity to deviations from design intent for multistage HLHM compressors. What one cannot see from such descriptions, and what is not well-defined in quantitative (and in some cases, qualitative) terms, are the different effects which arise from *blade row coupling* (i.e., blade row interaction) and which can become of import in this flow regime. The research results presented and discussed would thus center on defining: (i) what specific features of blade row coupling are important for HLHM compressors, (ii) what is their quantitative importance, and (iii) what are the basic dynamic scalings that capture this importance.

Figure 3.1, which categorizes compressor design in terms of Mach number versus design point stage loading provides a venue for discussion. Four categories of compressor stages

---

[1] By high Mach number stage we mean core compressor stages that operate at conditions with the flow supersonic over most of the span in a flow regime in which the properties of the passage flow are sensitive to small changes in inlet or exit conditions.

are shown, from low-loading, low-speed (type 1) to HLHM (type 4). Categories 2 and 3 are notional, and we thus contrast types 1 and 4 in terms of blade row coupling and effects on performance. For compressors in flow regimes represented by type 1 (and presumably to a large extent for types 2 and 3) the effects that have to do with multiple blade rows have been addressed and quantified. For example, Smith (1993) states that "multistage turbomachines have increased performance when the axial gaps between blade rows are reduced", presents a mechanism for a major part of this increase

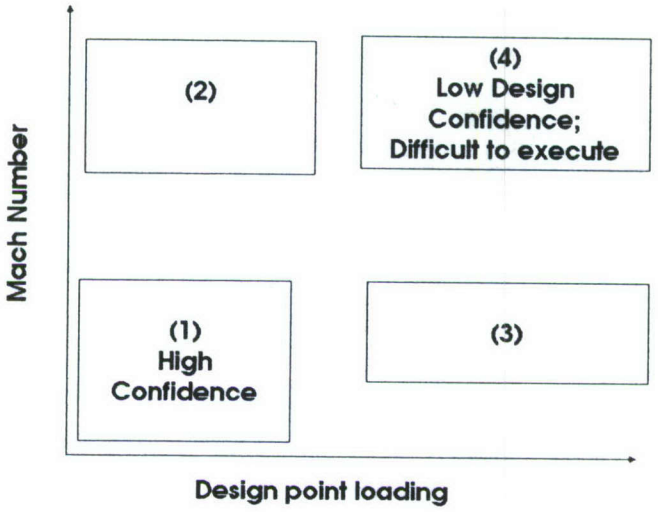

Figure 3.1: Notional classes of compressor design in Mach Number vs design point loading space.

(reversible work transfer to a wake as it passes through a succeeding blade row and consequent decrease in mixing losses) and quantifies the effect with a simple model. Computations on this point (Valkov and Tan, 1999) show agreement with this idea. The effect of tip leakage flow on succeeding stages has also been quantified for this regime (Valkov and Tan, 1999; Sirakov and Tan, 2003). For such stages, therefore, the effects have not only been addressed to a large extent, but their effect on machine performance has been estimated.

The observation, however, is that this situation is not true for compressors in flow regimes of type 4. The difficulties that the technical community has experienced in implementing designs in this regime is one indication. A further indication may be seen in the data in Figure 3.2 (Hetherington and Moritz,1977), which shows performance from a multistage compressor at two speeds. The data are for two different blade spacings. At the lower speed there is a slight increase in efficiency and pressure rise at the smaller blade spacing in agreement with the computational simulations referred to above and with other low speed experimental results (Smith, 1970; Mikolajczack, 1977). At the higher speed shown, however, there is a decrease in performance with the smaller spacing, i.e., a *qualitatively* different behavior. Further the magnitude of the change is much larger than at the lower speed.

One plausible reason for the qualitative change is simply that there are new effects that

occur at high speed. An example[2] is unsteady interaction of shock systems with shear layers (e.g. shocks propagating upstream from a rotor which affect the behavior of shear layers both within and downstream of the stator row). This mechanism has been shown to result in the thickening of the shear layers, increase in flow blockage (analogous to boundary layer displacement thickness), and consequent additional entropy generation and lowering of efficiency (Gorrell and Okiishi, 2003; Gorrell *et al.*, 2003).

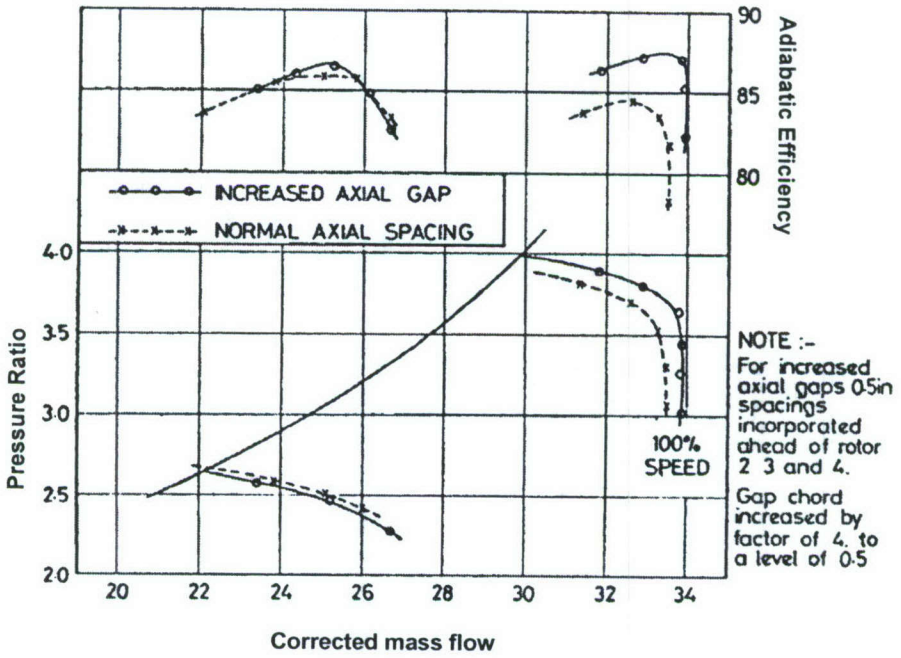

Figure 3.2: The effect of axial spacing on the performance of a 4-stage high pressure compressor (Hetherington and Moritz, 1977).

There is another, and different, cause that can be suggested, however. This is the interaction of several phenomena, which are understood in isolation but whose combined effect can give rise to qualitatively different behavior at high Mach numbers and loading. At Mach numbers near unity, the influence of even small changes in flow area (A/A*) and stagnation pressure is marked[3]; small changes in blockage or loss affect not only a particular blade row but can also cascade through a core compressor to alter the stage matching in a major way. Put another way, in the flow regimes of interest, apparently small changes in either flow blockage and/or loss can have a major influence on the mass flow capacity, the stage matching, and thus the performance of such machines. As such, the understanding, empiricism, and guidelines which apply well to machines of lower Mach number and loading may not apply to HLHM compressors.

The category of unsteady aerodynamic effects is of this type. In terms of performance their time mean impact enters as a quadratic non-linearity through terms such as $\langle \overline{u'u'} \rangle$,

[2] This is only one example and not necessarily the root cause of the difference in Figure 2.
[3] For example, at a Mach number of 0.9, a change in area of less than 1% causes the flow to choke.

where u′ is a typical velocity variation and the overbar denotes a time average. Even for large velocity variation magnitudes (10%), the time average effects will be only of order 1%. The stiff behavior of transonic flow, however, means there is leverage to create much larger variations in Mach number and flow angle. Further, the pressure fluctuations imposed on an upstream row (by a downstream row) are enhanced as the Mach number rises or the blade loading increases; not only the ability to alter the flow, but also the forcing that is applied, increases.

The research presented in this document is aimed at resolving aspects of unsteady phenomena that impact, in a substantive manner, the performance of high stage loading, high Mach number (HLHM) compressors. This document is organized as follows. We first described the overall approach and framework taken for addressing the scientific issues; here we will also present results from work by Gorrell *et al.* (2003) to demonstrate the adequacy of the tools used and of the AFRL research compressor as the HLHM compressor. Computed results on the selected HLHM compressor are presented to illustrate how a new physical mechanism (that involves unsteady interactions between blade-rows in HLHM compressor) is discovered. The thought process and the steps taken to quantify the impact of the newly discovered mechanism on rotor performance are next described; these entails designing and implementing additional computational experiments so that the causal link between rotor performance change and the physical mechanism can be established on a rigorous basis. A steady flow model that captures the time-average impact of the new physical mechanism is developed followed by using it to establish the basic fluid dynamic scalings that characterize the effects of coupling between blade rows. Finally we state the main conclusions and implications of the research.

4.0 Research Questions and Technical Approach

The specific research questions that were addressed are:

1. What flow changes are due to unsteady interactions between shock waves and shear layers (viscous layer on solid surfaces, wakes)?
2. How are these changes connected to: (i) peak efficiency and (ii) peak pressure rise of HLHM compressors (i.e. what is the impact of high loading and high Mach number on efficiency potential and why, in the sense of what mechanism is responsible, does this occur)?
3. What are the basic fluid dynamic scalings that characterize the effects of coupling between blade rows?
4. What levels of model are needed to appropriately capture these effects on the performance HLHM compressors?

The approach taken consists of assessing physical information at three different levels:

i) Detailed unsteady flow processes within the blade rows,
ii) Consistent assessment of the time-mean footprint of these processes, and
iii) Impact on overall stage characteristics (efficiency and peak pressure rise capability).

There are many different length and time scales in turbomachines, with a corresponding spectrum of unsteady processes. Assessing information at these three different levels enables us to determine which of these are important, and to define explicit causal links between flow details and overall metrics – this in essence is a key aspect of the overall framework of approach.

The unsteady three-dimensional flow at the rotor-stator blade passage level includes details of flow processes such as unsteady interactions of shear layers (wakes and viscous layers) with shocks, and unsteady fluctuation in the leakage flow in response to flow unsteadiness from adjacent blade rows. Of interest here are local regions of entropy production, as well as regions in which the flow changes are such as to cause additional entropy increase downstream. At this first level the fluid mechanic processes are most visible but their effect is not.

The second level is thus assessing the time-mean footprint of the unsteady processes. While the time-average flow can be computed from the unsteady three-dimensional flow via time-averaging over several cycles of blade-passing time periods, to determine the time-average impact of the unsteady interactions we need to define an analogous steady flow to which the time-average flow can be compared[4]. One can think of this comparison, posed in a consistent manner, as asking the question "How would the flow be different if the unsteadiness were absent?"

The third level of information is essentially the overall blade row performance quantities such as efficiency and flow blockage (a measure of the degradation in the pressure rise capability of the blade passage). Efficiency can be directly linked to the entropy production (or the potential entropy production, for example in non-uniformities that are not yet mixed out). Procedures for extracting normalized flow blockage across a blade passage have been developed and used in the work reported by Khalid *et al.* (1999) on tip clearance flow, Shum *et al.* (2000) on centrifugal impeller-diffuser interaction, Sirakov and Tan (2003) on unsteady wake and tip clearance blade effects on stator performance, and by Shabbir and Adamczyk (2004) for casing treatment operation. Comparison of the normalized blockage and entropy increase extracted from the time-average flow to that from the equivalent steady flow enables direct identification of the impact of specific flow processes. In sum, the progression through these different levels provides a means of (and a traceability for) identifying the flow features that set the achievable stage efficiency and pressure ratio.

Numerical calculations have been implemented to: (i) answer the above research questions; (ii) determine the entropy generating mechanisms responsible for the change

---

[4] There is no unique way of defining an "equivalent" average steady flow from an unsteady flow field (or an equivalent one-dimensional average from a spatially non-uniform flow). There are five conservation principles (mass, three momentum, and energy) so that the averaging process necessarily means that some variables will not be captured. For example, if each variable of interest is time-averaged separately, the resulting averaged steady flow field is inconsistent; the average stagnation pressure from the unsteady solution is different than the stagnation pressure calculated from the averaged Mach number and static pressure. There are, however, approaches which retain the features that are most relevant (Greitzer *et al.*, 2004].

in compressor performance with axial blade-rows spacing. The numerical calculations consist of sets of three-dimensional and two-dimensional unsteady simulations of flow in a HLHM compressor stage described in Gorrell *et al.*(2003, 2005).

The computational fluid dynamics (CFD) code used for the numerical simulations is described in Section (4.1) and the HLHM compressor configuration in Section (4.2).

4.1 Numerical Tool

Numerical simulations were conducted using MSU Turbo Version 4.1 [Chen *et al.* (2001)], an unsteady, three-dimensional, viscous code that solves the Reynolds Averaged Navier-Stokes (RANS) equations. The equations are solved in the reference frame of each blade row. The code employs a finite volume solver, with a k-ε turbulence model. Communication between blade rows in their respective reference frames occurs across a sliding plane that interpolates information from one blade row to the other.

To reduce computer time and memory required to perform the numerical experiments, temporal phase lag boundary conditions were used [Erdos *et al.*(1997), Chen *et al.*(1994, 1998), Wang *et al.*(2004)]. Temporal phase lag boundary conditions rely on the assumption that the flow field associated with two interacting blade rows has a temporal periodicity related to the blade count of the blade rows. More specifically, the flow field within the blade passage will repeat itself every time the relative position of the adjacent blade row is the same. The phase lag approximation permits the replacement of a full wheel or spatially periodic computation by a single blade passage within each blade row. The compressor stage used (see Section (4.2)) has 24 stator and 33 rotor blades. If periodic boundary conditions were used, a sector with 8 stator blades and 11 rotor blades would be required, implying much more computational time and computer memory than simulations with the temporal phase lag approximation. Using the phase lag approximation, a full wheel can be constructed at any instant in time using the computed flow field of the individual passage from previous instants in time. Details of the full wheel reconstruction are given by Wang and Chen (2004).

An assumption associated with the use of phase lag boundary conditions is that the lowest frequency of any important unsteady phenomenon is the blade-passing frequency of the adjacent blade row. For example, vortex shedding, rotating stall, or flow separation that is at a lower frequency than the blade passing frequency would not be captured. Use of the phase lag boundary condition is an appropriate approximation for unsteady blade row interactions where the frequency of unsteadiness in one blade row is dominated by the adjacent blade row passing frequency. The results from phase lag computations and experiment have been compared in the work by Gorrell *et al.*(2005), and the phase lag approximation captured the flow features that arise from the blade row interactions, including the vortex shedding from the inlet guide vanes due to the impingement of the rotor shock on the vane.

Uniform stagnation pressure and temperature are specified at the inlet of the computational domain. For three-dimensional simulations, at the exit of the

computational domain, the static pressure at the hub is specified, and simple radial equilibrium is used to specify the radial distribution of static pressure. For the two-dimensional simulations, the static pressure is specified at the exit. The convergence criteria was that the time-averaged mass flow rate at the vane row inlet and at the exit of the domain were within 0.1% of each other, and that the efficiency and mass flow were periodic with blade passing frequency.

MSU Turbo solves the flow field using primitive variables at cell centers. The MSU Turbo output data is therefore chosen to be the values at the cell center. Visualization of the output was accomplished with the post processing codes developed at the MIT Gas Turbine Laboratory by Villanueva (2006).

4.1.1 Time Discretization and Time-Averaging

The number of time steps for each blade period was chosen based on the desired temporal resolution of the blade row interactions. The frequency of unsteadiness within one blade row is determined by the blade passing frequency of the adjacent blade row, and resolving twenty harmonics of the blade passing frequency should well capture the flow features deriving from unsteady blade row interactions, including vortex shedding. According to Nyquist's theorem, a harmonic must be sampled at least twice per cycle in order to be resolved, so 40 samples were taken for one blade-passing period. In the vane/rotor configuration studied here, the rotor blade passing frequency in the vane reference frame is higher than the vane blade passing frequency in the rotor reference frame. The vane blade row simulation employed a time increment equal to $1/40^{th}$ of the rotor blade passing period, so the vane blade row is resolved in 40 time steps and the rotor blade row is resolved in 55 time steps (based on the vane to rotor blade ratio of 8:11).

Within the MSU Turbo code, specifying a small number of time steps requires more iteration at each time step to reach convergence; more time steps means less iteration. The number of time steps chosen was based on experience gained in the simulations conducted by Gorrell (2006), and is given in Table 4.1. By choosing a larger number of time steps, the solution of the flow field captures more harmonics than required, achieving greater accuracy.

Instead of time-averaging over one blade period using the computed results at every time instant (based on the number of time steps per period in Table 4.1), the unsteady flow field signature is captured up to the twentieth harmonic of the blade passing frequency. The vane blade row is time-averaged over 40 time instants and the rotor over 55 time instants, both at increments of four time steps apart. In the two-dimensional computations, the vane to rotor blade ratio is simplified to 2:3 (as will be discussed in Section 6.2), and the rotor is averaged over a total of 60 time instants.

4.2 HLHM Compressor Stage: AFRL Stage Matching Investigation Compressor

The HLHM compressor stage geometry is based on that used in the AFRL (Air Force Research Laboratory) 'Stage Matching Investigation' (SMI) rig shown in Figure 4.1; it is designed to study changes in performance with variations in axial blade row spacing for a highly-loaded, high Mach number compressor. The rig consisted of three blade rows: a wake generator or inlet guide vanes (IGV), a rotor and a stator. It was also run as a vane and rotor-only combination [Gorrell *et al.*(2003, 2005)]. The latter configuration is studied for two axial blade row spacings, denoted as "close" and "far", and given in Table 4.2.

Table 4.1: Number of time steps per period used in MSU Turbo Code.

Blade row	3D Simulations	2D Simulations
Vane	220	240
Rotor	160	160

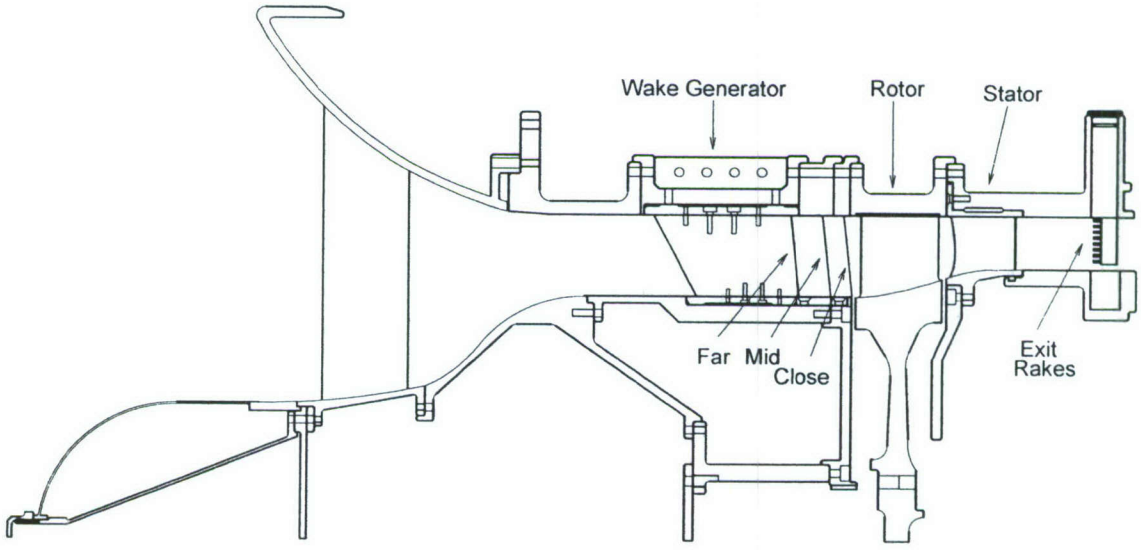

Figure 4.1: Stage matching investigation (SMI)rig layout (Gorrell et al., 2003).

Table 4.2: Axial blade row spacing L for close and far configurations, normalized by the axial rotor chord length c_x.

Spacing	L/c_x (mean)	L/c_x (hub)	L/c_x (tip)
Close	0.22	0.13	0.27
Far	0.86	0.80	0.95

The straight vane blades are designed to emulate the typical loss profile from a front stage stator in a high speed axial compressor. Details of the vane design are given by Chriss *et al.* (1999). The aerodynamic design parameters for the rotor are given in Table

4.3. The rotor tip clearance is 0.6% of the chord. The ratio between the number of vanes and rotor blades is 8:11.

Table 4.3: SMI Aerodynamic Design Parameters [Gorrell et al. (2003)].

Parameter	Rotor
Number of blades	33
Aspect Ratio (average)	0.961
Inlet Hub/Tip Ratio	0.750
Tip speed, corrected m/s	341.37
RPM	13509.0
M_{rel} LE M_{rel} Hub	0.963
M_{rel} LE Tip	1.191
LE Tip Dia., m	0.4825

The grid was created using the Average Passage Grid (APG) generator of Beach (2003). Gorrell *et al.* (2003) have determined that the grid provides sufficient resolution to capture the vortex shedding by comparing the numerical results to DPIV measurements [Gorrell *et al.* (2005)], and their grid was used for the calculations described here. The number of grid points for both the vane and rotor are given in Table 4.4. Additional details of the grid are provided by Turner et al. (2005).

Table 4.4: Number of grid points in axial, radial and pitch-wise directions for the three-dimensional calculations.

Blade row	Axial	Radial	Pitch-wise
Vane close	138	71	61
Vane far	230	71	61
Rotor	189	71	81

As was noted in Section (3.0), Gorrell *et al.* (2003) examined the effect of blade row spacing on performance for an axial vane row/rotor configuration. Specifically experiments were performed using SMI rig for three different inter-blade row axial spacings, having a mean (hub-to-tip) value of 13%, 26%, and 55% of the vane chord [Gorrell *et al.* (2003)]. The experimental measurements in Figure 4.2 show that the pressure ratio and efficiency are consistently lower for the close spacing than for the far spacing. The pressure ratio and efficiency were based on measurements at the inlet and at an exit plane 0.9 axial rotor chords downstream of the rotor trailing edge. Gorrell et al. (2003) inferred from the SMI rig measurements that choking mass flow rate, pressure ratio and efficiency all decreased as axial spacing was reduced [Gorrell *et al.* (2003)].

Unsteady CFD simulations (using MSU Turbo [Chen et al. (2001)]), conducted for the closest and farthest spacings of the SMI rig, enabled identification of a loss generating mechanism within the vane row passage [Gorrell *et al.* (2003)]. Oblique shock waves that originate from the rotor intersect the upstream vane row as they sweep past, giving rise to shock waves that propagate upstream along the vane surface, as shown in Figure 4.3. In the closer blade row spacing, the shock wave becomes perpendicular to the flow

direction and forms a normal shock, giving a higher entropy increase than for an oblique shock (Figure 4.3a). For the farther blade row spacing, the rotor shock is a weak compression wave at the vane trailing edge, and there is no normal shock in the upstream vane passage (Figure 4.3b)

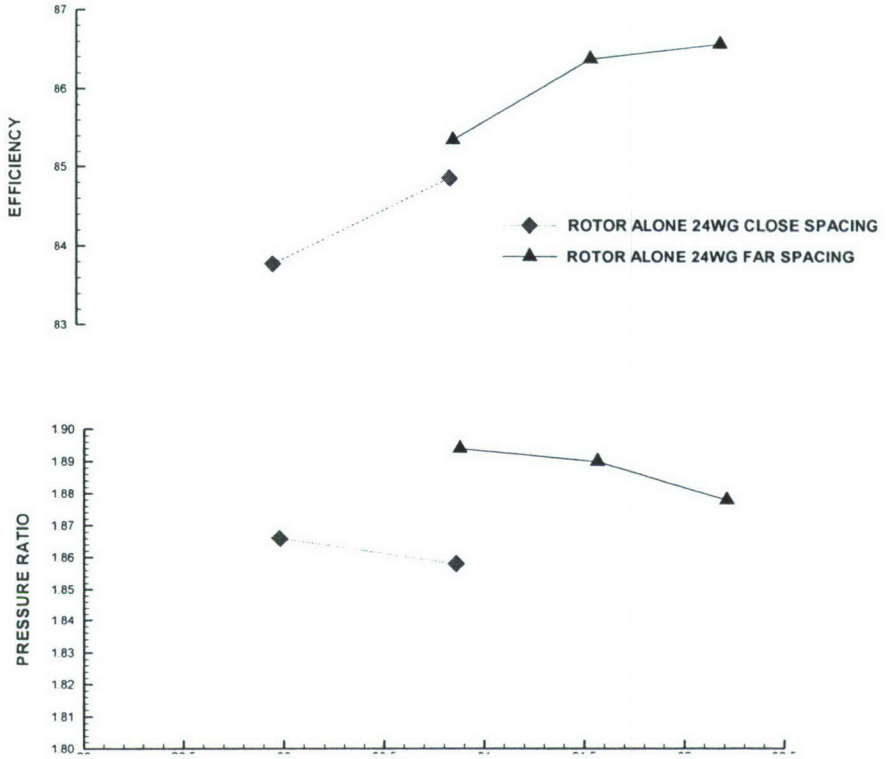

Figure 4.2: Vane/rotor-only performance from experiment, 100% speed. [Gorrell (2001)]. Both pressure ratio and efficiency decrease as blade-row spacing is reduced from 0.86 ("far") to 0.22 ("close") axial rotor chord length.

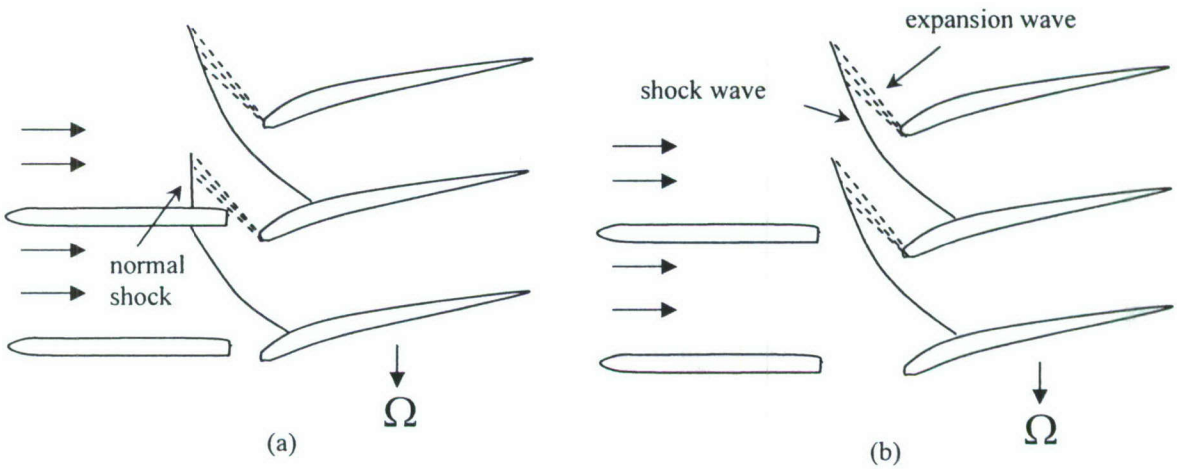

Figure 4.3: Comparison of wave configurations between the (a) closest and (b) farthest blade row spacing used in the SMI rig.

The entropy increase, from the inlet to the vane row trailing edge plane, was 12% higher for the closest blade row spacing configuration than for the farthest spacing at the same mass flow rate. Gorrell et al. (2003) attributed the additional entropy increase by the vane trailing edge to the normal shock in the reduced spacing, but a direct link between the two was not made. Furthermore, the entropy rise from the normal shock alone was not compared to the total shock losses or to the overall losses for the stage to determine if the normal shock was the main source of the difference in entropy generation for the different blade row spacings.

The efficiency, mass-averaged total pressure ratio, and mass-averaged total temperature rise, obtained from the CFD simulations, for the two configurations at the same corrected mass flow, are given in Table 4.5. The adiabatic efficiency η is calculated as:

$$\eta = \frac{TR\left(\exp\left(-\frac{\Delta s}{R}\right)\right)^{\frac{\gamma-1}{\gamma}} - 1}{TR - 1}, \qquad (4.1)$$

where the stagnation temperature ratio TR and entropy rise Δs are mass- and time-averaged over the selected measurement plane. The stagnation temperature rise, stagnation pressure ratio, and efficiency are lower for the close spacing configuration than for the far spacing configurations; the computed trend is thus in accord with the measured trend.

To summarize the AFRL SMI compressor stage can be used to addressing the research issues of relevance to the HLHM compressor and the MSU Turbo is an adequate computational tool for simulating unsteady three-dimensional flow in the AFRL SMI stage. The central theme of research presented here is on unsteady flow features *downstream* of the rotor leading edge that impact compressor perfromance; this is in *distinct contrast* to previous work [Gorrell *et al.* (2003)] on examining unsteady flow features *upstream* of the rotor leading edge.

Table 4.5: Mass flow rate, mass-averaged total temperature rise, mass-averaged total pressure ratio, and adiabatic efficiency from three-dimensional calculations for far and close spacing configurations. Exit values are time-averaged on a plane 0.9 axial rotor chords downstream of the rotor trailing edge.

Spacing	Mass flow (kg/s)	Mass-averaged T_t rise	Mass-averaged p_t ratio	Efficiency η
Close	14.89	0.221	1.846	0.891
Far	14.89	0.219	1.872	0.897

4.3 Overall Summary of Approach

The MSU Turbo is used to simulate three-dimensional unsteady flow field in the AFRL SMI compressor stage based on the grid and/or additional modifications of the grid provided by Gorrell (2001) for different vane-rotor axial spacing and different rotor tip

clearances. Post-processing techniques have been developed to provide a quantitative means for identifying the flow processes that set the achievable efficiency and pressure rise capability. This entails processing and interrogating flow field at the three different levels discussed at the beginning of this section: (i) detailed unsteady flow processes within the blade rows; (ii) consistent assessment of the time-mean footprint of these processes in terms of loss generation and flow blockage generation; and (iii) impact on overall stage characteristics (efficiency and pressure rise capability).

As an illustration consider assessing the flow fields for two configurations (e.g. the far spacing versus the close spacing) to determine, for instance the difference in entropy generation. To identify the cause for this difference, we compute the local dissipation function [Greitzer, *et al.* (2004)]

$$\phi = \frac{\tau_{ij}}{T}\frac{\partial u_i}{\partial x_j} + \frac{1}{T}\frac{\partial}{\partial x_i}\left(k\frac{\partial T}{\partial x_i}\right) \qquad (4.2)$$

(τ_{ij} denotes the stress tensor, k the thermal conductivity, u_i the velocity component, T the temperature, and x_i the co-ordinate) which appears on the right hand side of the transport equation for entropy *s* [Greitzer, *et al.* (2004)] (see equation (5.3) below). The distribution of dissipation allows the dominant loss mechanisms to be identified (i.e. what flow process is responsible for the observed high dissipation and or difference in dissipation between the two configurations?). A hypothesis on the causal link between the flow process and the loss generation can then be formulated. Additional numerical experiments (which could be two-dimensional unsteady calculations and/or even steady state calculations depending on the hypothesized physical process) are designed and implemented to prove the formulated hypothesis as well as to establish the scaling in terms of the relevant key controlling parameters.

It will be shown in Section 5 to 8 that the interrogation of results from unsteady three-dimensional simulations of flow in the HLHM compressor stage first leads to the formulation of a hypothesis. A set of well-designed unsteady two-dimensional computational experiments is used to assess the hypothesis. The time-average response of the rotor is also assessed using steady-state computations of a flow model for the compressor stage. Then the flow in a two-dimensional diffuser subjected to a wake and jet is used to provide a physical context explaining the response of the rotor performance to the discrete wakes from upstream blade-row. The flow model is used to establish the scaling of rotor performance change in terms of the key controlling parameters. Finally the findings extracted from two-dimensional computational experiments and flow model are used to *estimate* the bounds of the impact of unsteady IGV-rotor interactions on rotor performance change in the three-dimensional flow situations.

In the next Section the far spacing and the close spacing configurations described above are further assessed to determine where the differences in entropy generation arise.

5.0 Quantification of Sources for Entropy Generation

The differences between the performance for the "close" and "far" configurations, as determined from three-dimensional computations, were described in Section 4.2. Gorrell et al. (2003, 2005) described two possible mechanisms to explain the lower performance in the close spacing configuration compared to the far spacing. The first was the oblique shock increasing in angle (towards the direction perpendicular to the free stream) inside the vane row [Gorrell *et al.* (2003)]. The second was the entropy associated with the shed vortices as they are formed at the vane trailing edge when the blade row spacing is reduced [Gorrell *et al.* (2005)].

Gorrell *et al.* (2005) have employed CFD simulations with a more refined grid, as well as Digital Particle Image Velocimetry (DPIV) measurements to examine the discrete vortices shed at the vane trailing edge that exist because of the interaction between the rotor shock and upstream stationary blade row. Within one rotor passing time, two discrete counter-rotating vortices were found to be shed at the vane trailing edge. The formation of these vortices can be explained as follows. When the rotor shock intersects the vane trailing edge, a pressure gradient is established along the surface of the blade, resulting in a flux of vorticity from the wall into the fluid, and a net circulation established around the blade. The vorticity generated on the vane is shed from the trailing edge to form a vortex. As the rotor shock moves past the vane trailing edge, the pressure gradient along the vane decreases, as does the net circulation, and a discrete vortex with opposite circulation to the previous one is shed. A vortex street which is "locked" to the rotor passing is thus formed downstream of the vane trailing edge.

From the above arguments, as the blade row spacing is reduced and there is a stronger shock impinging on the upstream blade row, there will be a larger pressure gradient and a larger vane circulation. The length scale associated with the vortices is related to the blade thickness, and thus, a larger vane circulation results in greater vorticity within the shed vortices. The shed vortices not only contain more vorticity, but are also observed to have greater entropy as blade row spacing is reduced.

Gorrell et al. (2005) developed an analytical relation for the shed vorticity as a function of vane geometry and rotor shock strength which correlated well with their computational results. The vorticity within the shed vortices is given as:

$$\omega = \left(\frac{4}{\pi \tan\phi}\right)\left(\frac{\Delta p}{\bar{p}}\right)\left(\frac{\bar{p}}{\dot{m}}\right)\left(\frac{1}{\lambda}\right). \qquad (5.1)$$

In equation (5.1), ϕ is the shock angle (see Figure 5.1), $\Delta p/\bar{p}$ is the pressure rise across the shock, $\bar{p}$ is the average of the pressures ahead and behind the incoming shock, $\dot{m}$ is the mass flow rate, and λ is the trailing edge blockage, i.e the ratio of trailing edge thickness to pitch. A model by Morfey and Fischer (1970) was used to calculate the shock strength, $\Delta p / \bar{p}$, as a function of rotor Mach number, axial flow Mach number, and ratio of the axial distance ahead of the rotor to rotor pitch.

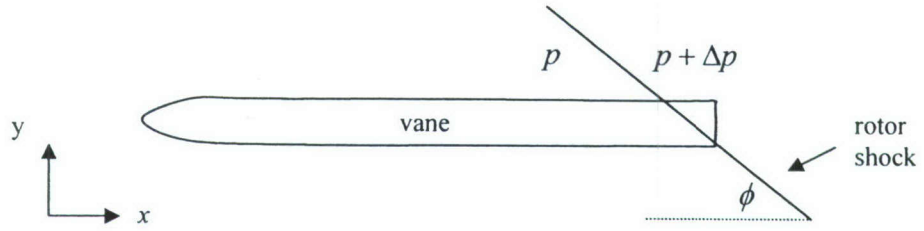

Figure 5.1: Rotor shock impinging on the upstream vane row causing a net loading on the blade, and the formation of shed vortices.

While the vorticity in the shed vortices was estimated, the entropy generation associated with the creation of the vortices and the additional losses as they are convected downstream, however, was not quantified. The loss associated with the vortices was also not compared to other loss generating mechanisms (such as shock waves) for the stage.

In summary, the entropy generation associated with vane vortices upstream of the rotor leading edge has not been compared quantitatively with the overall losses for the stage. In this Section, the dominant source of entropy generation that leads to the performance differences between the far and close spacing is identified and quantified, using a new numerical technique to calculate the local dissipation. In addition, a method to isolate entropy generation within shock waves is also developed.

5.1 Sources of Entropy Generation

To demonstrate where the entropy generation occurs in the two three-dimensional configurations, the entropy flux at different axial locations is presented in Figure 5.2[5]. The close spacing has a higher entropy increase than the far spacing within the rotor and downstream of the rotor, leading to a lower efficiency for the close spacing. The higher overall entropy rise throughout the domain for the close spacing occurs despite the fact that the entropy increase from the inlet of the domain to the rotor leading edge is lower in the close spacing than in the far spacing configuration.

The inference from the computed results of Figure 5.2 is that the two entropy-generating mechanisms described above, which occur upstream of the rotor, do not account for the reduced performance in the close spacing. These two mechanisms imply that the additional entropy generation in the close spacing occurs upstream of the rotor leading edge plane. If so, the entropy flux into the rotor would have to be higher into the rotor in the close spacing. This is not the case.

[5] In the figure, it should be noted that the physical distance between the vane trailing edge and the rotor leading edge is different for the far and close spacings.

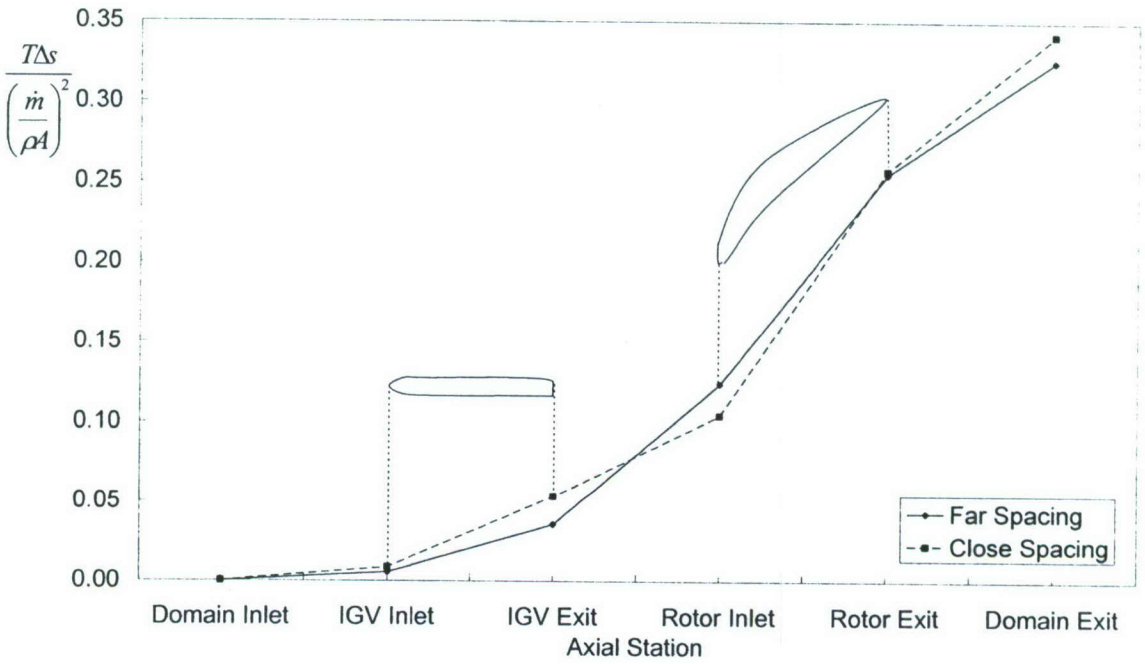

Figure 5.2: Entropy flux as a function of axial location for far and close spacing. Entropy values referenced to p_{ref} = 1 atm, T_{ref} = 300K.

To explain the larger entropy increase downstream of the rotor leading edge plane in the close configuration, the rotor shock and the shed vortices are examined. Losses associated with the shed vortices as they convect downstream have not previously been assessed. Figure 5.3 shows entropy contours from numerical simulations for far and close spacings at the mid-span radius. Entropy is non-dimensionalized as $T\Delta s/(\dot{m}/\rho A)^2$ and referenced to p_{ref} = 1 atm, T_{ref} = 300K; $\dot{m}$ is mass flow rate and A the area. In the close spacing, higher entropy is observed in the vortices at their inception than in the far spacing, as identified by Gorrell (2001). However, as these vortices move downstream, they diffuse and interact with the rotor boundary layer and wake, generating additional entropy. An issue to be addressed is whether the entropy generation associated with the shed vortices as they move through the blade passage is a major contributor to the total difference in entropy generation between the far and close spacing configurations.

Shock waves in rotor are another source of entropy generation. The shock wave location can be highlighted using the velocity divergence field. The continuity equation is:

$$\nabla \cdot \vec{u} = -\frac{1}{\rho}\frac{D\rho}{Dt}. \qquad (5.2)$$

$\vec{u}$ is the velocity vector and ρ the density. Regions of compression have a negative value of the divergence of velocity, and expansion regions have a positive value. Figure 5.4 is a contour plot of the divergence of velocity at the mid-span for both configurations. The divergence of velocity is non-dimensionalized by the tip speed (which is equal

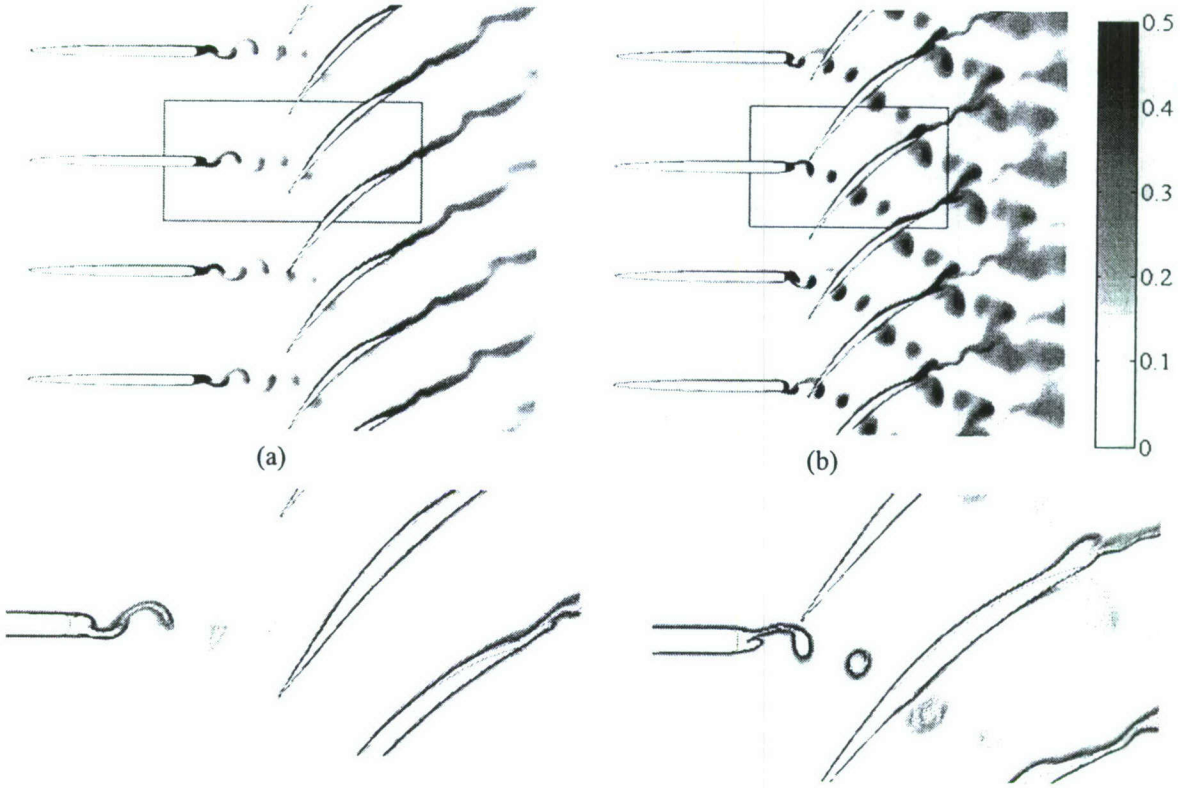

Figure 5.3: Entropy contours at mid-span for (a) far spacing, (b) close spacing. All plots are of the same scale. The lower contour plots correspond to the boxed regions in the upper plots, and have 20 evenly-spaced intervals.

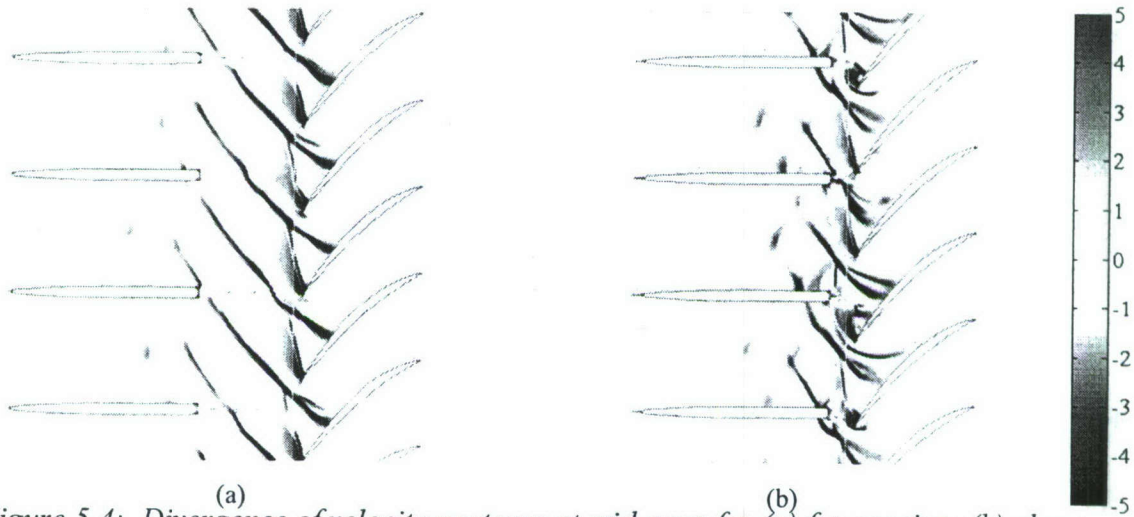

Figure 5.4: Divergence of velocity contours at mid-span for (a) far spacing, (b) close spacing. Blue regions describe regions of compression, and red describe regions of expansion.

to $\sqrt{\gamma RT_{ref}}$, where γ is the ratio of specific heats and R the specific gas constant) and the axial rotor chord length. The shock structure is different for the two spacings, and is more unsteady with the close spacing compared to the far spacing. The entropy generation within the rotor due to shock waves is quantified below.

5.2 Computation of Local Dissipation

In this section, the numerical implementation of the equations to calculate the local entropy generation is presented. The entropy increase within a specified control volume is then quantified to determine where differences exist between the close and far spacing configurations.

The rate of entropy change of a fluid particle is:

$$\rho\frac{Ds}{Dt}=\frac{1}{T}\tau_{ij}\frac{\partial u_i}{\partial x_j}+\frac{1}{T}\frac{\partial}{\partial x_i}\left(k\frac{\partial T}{\partial x_i}\right). \tag{5.3}$$

The two terms on the right-hand side of equation (5.3) represents entropy changes due to viscous effects and heat transfer, respectively. The former is irreversible, but the latter includes both reversible and irreversible changes. All irreversible processes in this report will be referred to as *dissipative processes*, where entropy generation is equivalent to lost work. The "physical dissipation" will be defined as the entropy generation due to the action of viscosity and irreversible heat transfer, calculated from the gradients in velocity and temperature. For a control volume encompassing the rotor shock waves, as in Figure 5.5, reversible heat transfers across the control surface are negligible compared to entropy generation within the control volume. Therefore, the physical dissipation should (theoretically) capture the entropy generation across a shock wave.

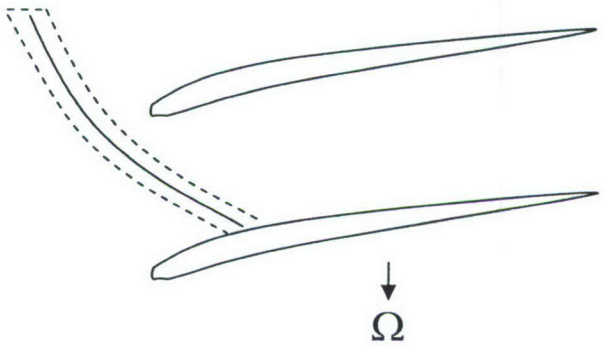

Figure 5.5: Dashed line represents a control volume around the rotor shock wave (Ω denotes rotor blade speed).

However, a problem arises when the physical dissipation is computed from gradients in velocity and temperature in the region of the shock wave, because the grid is not dense enough to accurately compute the spatial derivatives. Therefore, instead of computing the entropy generation from gradients in velocity and temperature in the right-hand side of

equation (5.3), the local entropy rise can be computed from the left-hand side of equation (5.3) directly, which will be referred to as the "computational dissipation," i.e.

$$\frac{\partial(\rho s)}{\partial t} + \nabla \cdot (\rho \vec{u} s). \tag{5.4}$$

The first term in equation (5.4) represents the time-rate of change of entropy per unit volume. In the MSU Turbo code, it is calculated using a centered-difference scheme in time. The second term represents the net entropy flux for each computational cell. This is computed by interpolating fluid properties to each cell boundary to define the net entropy flux out of the cell volume at every instant in time.

The computational dissipation allows adequate evaluation of entropy generation in regions with shock waves because the entropy is calculated from primitive variables, which are obtained by solving the conservation equations in the MSU Turbo simulation. In the MSU Turbo code, the numerical scheme includes additional dissipation, other than the physical dissipation to accurately calculate entropy generation. This additional dissipation is referred to as "numerical dissipation." The total dissipation (or entropy generation) is therefore equal to the physical dissipation (computed from the gradients in velocity and temperature) plus the numerical dissipation (implemented by the code). As the grid mesh size goes to zero, the numerical dissipation also vanishes.

Using the new definitions for the calculated dissipation, the computational dissipation is equal to the sum of the physical dissipation, numerical dissipation, and the entropy changes due to reversible heat transfers across the control surface. As stated previously, these reversible heat transfers are negligible in the region of shock waves. They are identically zero if the bounding surface of the control volume of interest is adiabatic. The computational dissipation, when time-averaged and integrated over a specified control volume, is equal to the time-averaged net entropy flux out of that control volume. This is because the first term in equation (5.4) vanishes due to periodicity of the flow field, i.e.:

$$\frac{1}{\tau}\iint\left(\frac{\partial(\rho s)}{\partial t} + \nabla \cdot (\rho \vec{u} s)\right) dt\, dV = \frac{1}{\tau}\iint (\rho \vec{u} s)\cdot \vec{n}\, dA\, dt\,. \tag{5.5}$$

In Equation (5.5) τ denotes the time period, V the control volume, and $\vec{n}$ the unit vector normal to control surface A. When the computational dissipation is integrated over a control volume with an adiabatic surface, the computational dissipation should equal the entropy generation for that volume.

Where heat transfer terms are negligible, the computational dissipation should always be positive. Negative values, however, arise because the computational dissipation is calculated using a centered-difference scheme as opposed to the up-winding scheme used by Turbo. Entropy-generating flow features (e.g. shock waves, vortices) are associated with both positive and negative values of the computational dissipation that are located close together in the region of the flow feature. When the computational dissipation is integrated over a control volume that encompasses both the positive and negative values

of the computational dissipation associated with these flow features, the entropy generation is accurately captured.

The contribution of the physical dissipation and the computational dissipation can be assessed independently in regions that have both shock waves and shear layers. This allows us to determine how well the physical dissipation represents the actual entropy rise for a control volume. Figure 5.6 shows the entropy rise within a control volume defined from the vane trailing edge to a specified axial location and from hub to tip (these are adiabatic surfaces). Within the first 40% of the axial gap, which is the region in which the shed vortices are formed, the computational and physical dissipation are in good agreement, implying that the physical dissipation accurately captures the entropy generation associated with shear layers. After this point, the two dissipation schemes diverge, and the physical dissipation under-estimates the computational (i.e. actual) entropy flux. The divergence occurs because closer to the rotor, the shock wave is stronger and the physical dissipation is unable to resolve the spatial gradients associated with the shock wave. The inability of the physical dissipation to capture the shock entropy rise demonstrates the necessity to use the computational dissipation as the proper measure of entropy creation.

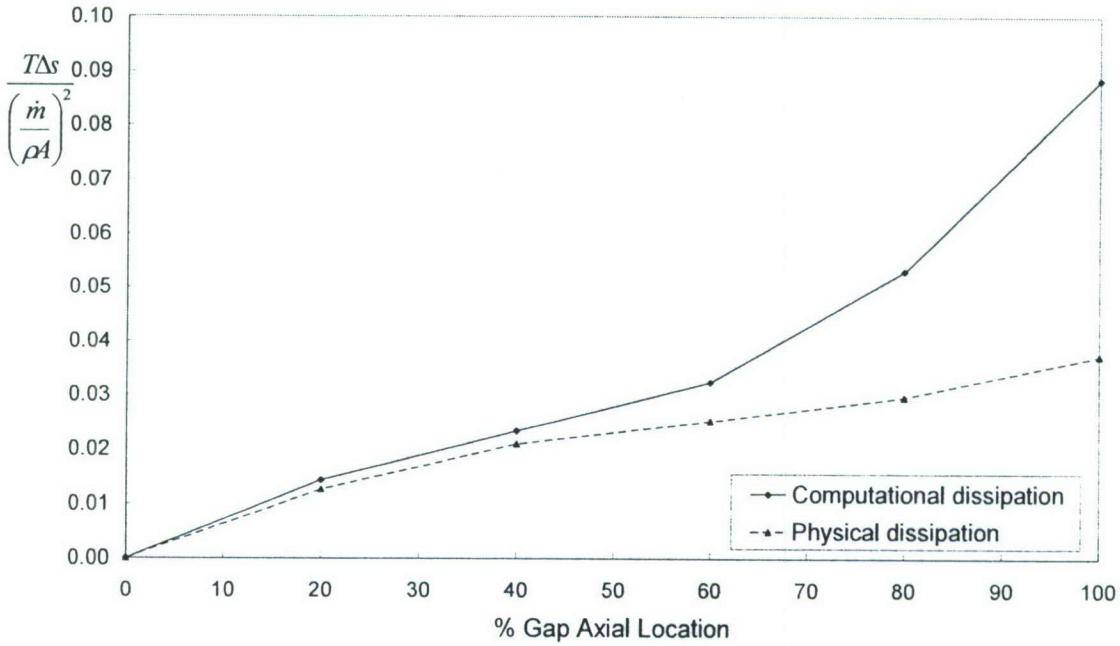

Figure 5.6: Comparison of entropy rise calculated from the computational and physical dissipation in axial gap for far spacing. Entropy values are calculated with respect to the vane trailing edge. Solid lines are calculated from the computational dissipation, and dashed lines from the physical dissipation.

5.3 Procedure to Compute Shock Entropy Rise

In Section 5.1, differences in the (unsteady) shock behavior were observed for the different configurations: the far spacing and the close spacing configuration. The

corresponding difference in entropy generation from the shocks will now be quantified. To isolate the shock waves computationally, the divergence of velocity is used as a marker and the shock waves are highlighted by marking regions where the divergence of velocity is below a specified threshold value.

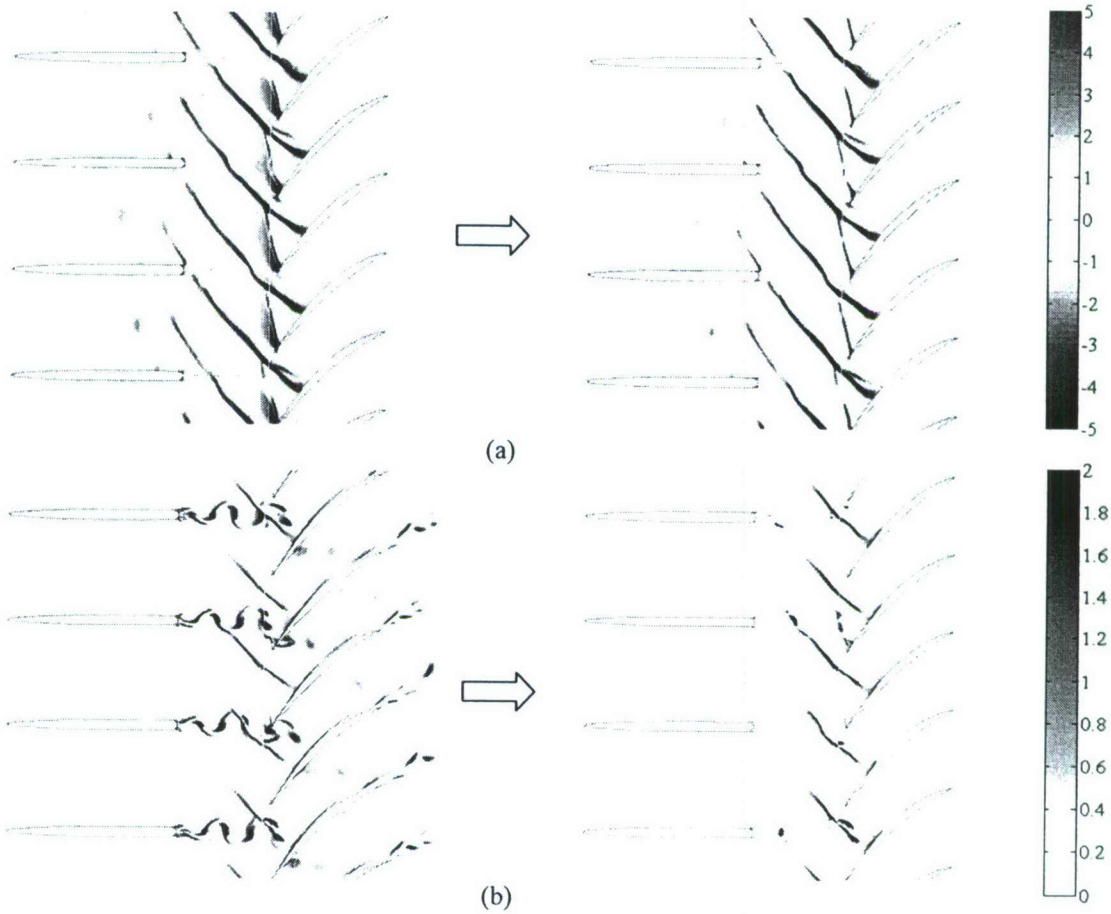

Figure 5.7: Isolating rotor shock waves: contour plots at the mid-span for the Far spacing where in (a) Shock waves are highlighted by specifying a threshold value of the divergence of velocity (here, the threshold is a non-dimensionalized value of -1), and in (b) Computational dissipation is specified in region of shock wave.

Figure 5.7 illustrates the procedure to isolate the entropy rise associated with shock waves. In Figure 5.7, two contour plots of the divergence of velocity are shown at the mid-span in the far spacing. On the left, the divergence of velocity is given everywhere in the flow field, and on the right, the divergence of velocity only in the shock region is plotted. Negative values of the divergence of velocity define compression regions, and the shocks (the dark blue regions) can be identified ahead of the rotor. To calculate the entropy rise across the shock wave, a control volume is placed around the shock wave. The geometry of the control volume around the shock wave is determined by specifying a threshold value for the divergence of velocity. If the divergence of velocity is below the threshold value at any cell, that cell is specified as part of the shock wave control volume. Implementing the above procedure of identifying the shock region is referred to as "masking", because the shock waves are essentially masked from the rest of the flow

field. In Figure 5.7b, positive values of the computational dissipation are plotted in the contour plot on the left. Negative values were not plotted because they would reduce the clarity of the figure, but are immediately adjacent to regions where the computational dissipation is positive. Negative values are important when integrating the computational dissipation to find the entropy rise associated with the shock wave, as described in Section 5.2. The computational dissipation is non-dimensionalized as $T(comp.dissip.)c_x/\rho(\dot{m}/\rho A)^3$, where *comp. dissip.* represents the quantity in equation (5.4). By applying the mask of the divergence of velocity, the computational dissipation in the shock region is isolated, as seen in the contour plot on the right of Figure 5.7b. Integrating the "masked" computational dissipation in space and time gives the entropy rise associated with the rotor shock.

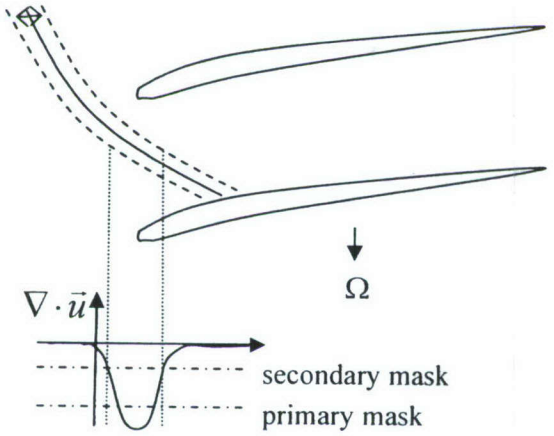

Figure 5.8: Schematic of the profile of divergence of velocity in shock region. A primary mask isolates the shock wave, and a secondary mask ensures the entire shock region is captured.

One issue in this procedure concerns setting the magnitude of the threshold. The shock wave encompasses a finite region within which the divergence of velocity can take on a range of values below the threshold value, as depicted in Figure 5.8. The choice of threshold value is critical. If it is too high, it can include cells associated with flow features unrelated to the shock. Therefore, a primary threshold value (called the primary mask) is used to identify the general location of the shock, and then a secondary threshold value (called the secondary mask) is applied to the immediate surroundings to ensure capture of the entire shock region. If the divergence of velocity is below the secondary threshold in the cells that neighbor the region where the primary mask is valid, those cells are also considered to be in the shock region. This ensures that the complete shock structure, and only the shock structure, is included in the mask and reduces numerical error when the primary mask does not capture the entire shock region.

To apply the above procedure, three parameters must be specified: the primary and secondary threshold values, and the number of neighboring cells around the cell where the primary mask is valid to evaluate the secondary mask value. The values for all three parameters, chosen to capture the entire shock region at all spans, were varied to test

sensitivity of the results. It was found that the value of each of the three parameters does not change the conclusion that the majority of the differences in entropy generation between configurations is not from shock waves. Table 5.1 shows the results from four values of the primary mask that were used to compare the contribution from inside and outside the masked region to the overall difference in rotor entropy rise between the far and close configurations. To encompass the entire shock region for all values of the primary mask in Table 5.1, the secondary mask was chosen to be -0.2, and was evaluated within a range of two cells around the primary mask.

Table 5.1: The difference in entropy generation within the rotor for the far and close configurations is divided into the differences inside and outside the masked (shock) region. The difference is measured for a range of primary mask values of the divergence of velocity.

$\nabla \cdot \vec{v}$ – primary mask	Mask	Outside Mask
0	27%	73%
-1	24%	76%
-1.5	14%	86%
-2	2%	98%

Over the range of primary mask values in Table 5.1, the close spacing has a higher entropy rise both inside and outside the masked region. The maximum difference in entropy rise between the far and close spacing within the masked region is 27% of the total difference. The rest of the difference in entropy increase is outside the shock region. Lowering the magnitude of the primary threshold reduces the computed contribution of the shock entropy rise to the total entropy rise, but the conclusion that the majority of the losses occur outside the shock region is unchanged, even with the magnitude of the primary mask set to zero. This conclusion holds when the end wall regions are removed from the control volume over which the computational dissipation is integrated, and in fact, the shock losses in the far spacing are measured to be higher than in the close spacing when the non-dimensionalized divergence of velocity is -2, as seen in Table 5.2.

Table 5.2: Results from Table 5.1, excluding the end wall region. A positive percentage value indicates that the close configuration has a higher entropy generation than the far configuration.

$\nabla \cdot \vec{v}$ – primary mask	Mask	Outside Mask
0	37%	63%
-1	23%	77%
-1.5	9%	91%
-2	-9%	109%

The conclusion is that the entropy generation due to shock waves is not the dominant mechanism responsible for the performance difference observed with changes in spacing. The main difference between the far and close spacing configurations must therefore be associated with differences in entropy generation from the vortices within the rotor blade passage.

The next Section focuses on these shed vortices and their effect on the overall stage performance as they propagate through, and interact with, the rotor.

6.0 Vortex Trajectory Within the Rotor

A change in axial inter-blade row spacing has two identifiable effects on the shed vortices from the upstream vane row: 1) a change in the strength of the vortices, and 2) an alteration in vortex trajectory within the rotor. The former is the increased circulation of the shed vortices as axial blade row spacing is decreased, as described by Gorrell *et al.* (2005). The second effect, the change in the relative location of the vortices in the rotor blade passage, is perhaps not as obvious. Interrogation of computed flow for the close spacing configuration on planes at two different radial locations shows a distinct difference in the vortex trajectories. This difference in vortex is elucidated in Figure 6.1 for two entropy contour plots of wake vortices from upstream IGV entering and traveling through a rotor row; Figure 6.1(a) shows the trace of vortex trajectory on a circumferential plane at midspan while that at 0.65 span is shown in Figure 6.1(b).

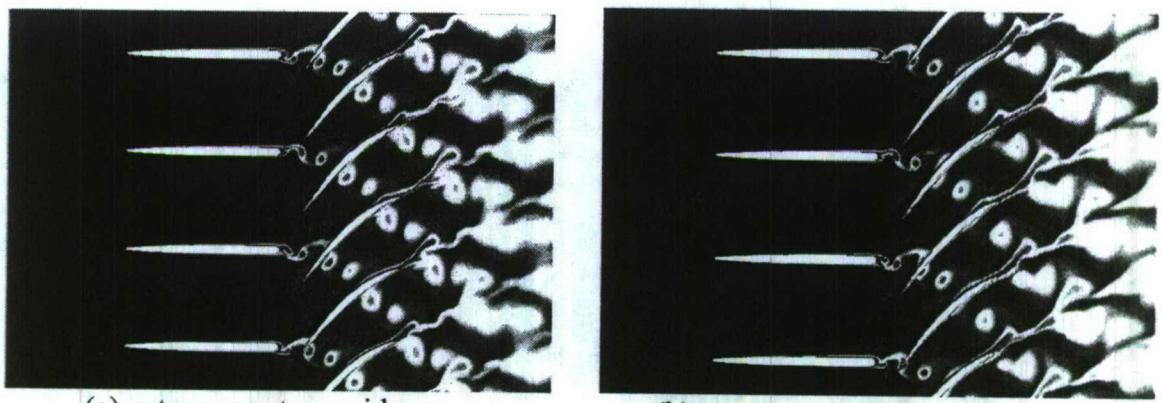

(a) entropy contour midspan (b) entropy contour at 0.65 span

Figure 6.1: *Entropy Contours elucidating the difference in the trajectories of IGV wake vortices traveling through the rotor blade-row at midspan in (a) and at 0.65 span in (b).*

The entropy contours of the IGV wake vortices in Figure 6.1 show a distinct difference in: (i) the pitchwise location (relative to the blade) at which the discrete vortices enter the rotor blade passage at midspan location from that at 0.65 span location; (ii) the trajectory of the wake vortices in the rotor passage of situation depicted in Figure 6.1(a) and in Figure 6.1(b); likewise a similar difference can be seen in the computed flow for far spacing and close spacing configuration shown in Figure 5.3. As noted in Section (5.0) within one rotor passing time, two discrete counter-rotating vortices are shed at the vane trailing edge; this is the rotor blade passing time which is invariant with radial/spanwise location. However the vane-rotor axial spacing changes with span so that the time taken by a discrete vortex to traverse from IGV trailing to rotor leading edge in the situation depicted in Figure 6.1(a) is different from that in Figure 6.1(b). The difference in the convective time scale of the discrete vortices (between the two situations in Figure 6.1) gives rise to the second effect, namely an alteration in vortex trajectory within the rotor.

The second effect, the change in the relative location of the vortices in the rotor blade passage, is illustrated in Figure 6.2, which conceptually shows vortex trajectories for two axial spacings. This Section focuses on the parameters that affect the vortex trajectory, and how the changes in trajectory affect stage performance.

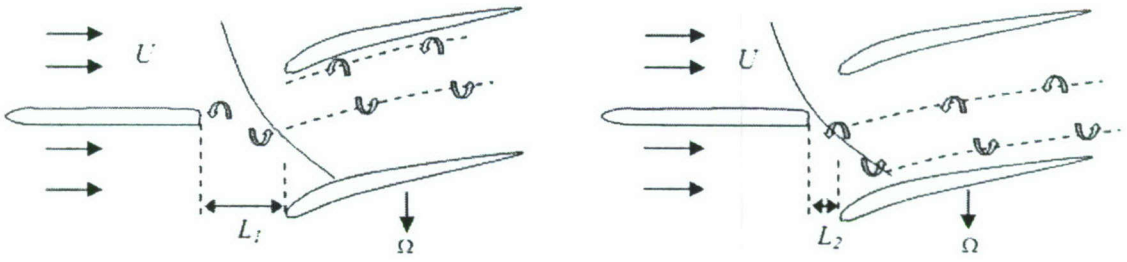

(a) (b)

Figure 6.2: Schematics in (a) and (b) show different vortex trajectories within the rotor passage due to different axial blade row spacing L.

6.1 Parametric Dependence of Vortex Trajectory within Rotor

Shed vortices from the upstream vane trailing edge move downstream across the axial blade row gap and then through the rotor blade passage. A key observation is that the pitch-wise location of the vortices within the rotor passage is defined by the pitch-wise location of the vortex when it crosses the rotor leading edge plane. For a given Mach number and blade geometry in this two-dimensional flow, the pitch-wise location of the vortices is a function of the ratio between two times scales: the time it takes for a vortex to travel the length of the vane-rotor gap, and one rotor period (i.e. the time for the rotor to move one rotor pitch). To elaborate, let the time origin, $t=0$, be the instant the vortex is shed. At this instant, the rotor is at a certain position with respect to the upstream vane row. As the vortex travels across the vane-rotor gap, the rotor moves from its position at $t=0$. Therefore, the relative location of the vortex in the rotor thus depends on how far the rotor has rotated in the time it takes for the vortex to travel the length of the gap.

Based on the above arguments, there are two time scales of interest. One is the convective time for a vortex to travel the length of the gap (τ), i.e.

$$\tau = \frac{L}{U} \tag{6.1}$$

where L is the gap length, and U is the mean axial velocity. The second is the rotor period, which is the time for the rotor to move one rotor pitch (τ'):

$$\tau' = \frac{2\pi / nblades}{\Omega} \tag{6.2}$$

where $nblades$ is the number of rotor blades, and Ω is the rotor rotational speed. The vortex trajectory within the rotor blade passage depends on the ratio of τ'/τ , except in the cases where

the ratios are integer multiples. An integer multiple of the time ratio (or similarly, a multiple of the rotor period τ') is equivalent to the rotor moving through that same multiple value of the rotor pitch, and the vortex trajectory is unchanged.

It should be emphasized that the vortex shedding from the upstream vane row is directly linked to the rotor blade passing frequency by the rotor pressure field. More specifically, the kinematics of the rotor shock impinging on the upstream vane row dictate that the vortex shedding from the vane trailing edge occurs at a frequency equal to the rotor blade passing frequency. The consequence of this relationship is that the rotor is at the same relative position to the upstream vane row when vortices of the same sign are shed.

The ratio of the two time scales, the convective time scale and the rotor blade passing period, defines a dimensionless parameter $B3$:

$$B3 = \frac{L\Omega}{U}\left(\frac{1}{2\pi / nblades}\right) \tag{6.3}$$

For a vortex shed from the vane trailing edge in a two-dimensional flow, a change in the parameter $B3$ (in particular the axial gap spacing L, which is the present variable of interest) results in a change in the vortex trajectory through the rotor.

The above discussion pertains to a two-dimensional flow. For a three-dimensional flow, a change in blade row spacing will result in a change in the vortex trajectory at every radial plane. At each radial span in an axial compressor, the vortex trajectory may be beneficial or detrimental with regards to performance. Altering the vortex trajectory at each radial span could lead to an enhanced stage performance. For example, the vortex trajectory within the rotor can be tuned at each radial span by changing the $B3$ parameter or the stagger angle of the blade.

6.2 Vortex Trajectories in the Unsteady Two-dimensional Computations

To assess the effect of a change in the vortex trajectory on rotor performance, unsteady two-dimensional calculations have been conducted, as outlined below.

A two-dimensional grid was generated using the blade geometry from the far spacing configuration three-dimensional grid at 65% span. This radial span represented the average stagger angle of the three-dimensional grid from hub to tip. The same code, MSU Turbo [Chen *et al.*(2001)], used for the unsteady three-dimensional calculations was used for the unsteady two-dimensional calculations. The geometry was created by placing two radial planes close together and at a large radius, R, so that $\Delta r/R$ was 0.17% (in the simulation, the radius R was made 110 times the original radius). The vane to rotor blade ratio was also changed, for simplicity, to 2:3. The configuration created using an axial spacing equal to the spacing at 65% span is referred to as far_{2D}. The configuration with the axial spacing reduced by 11% from far_{2D} will be referred to as $close_{2D}$. The axial spacing is 0.81 and 0.91 of the axial rotor chord length for $close_{2D}$ and far_{2D}, respectively.

The effect of a change in the shed vortex trajectory on performance was examined using the $close_{2D}$ and far_{2D} configurations. Section (6.1) describes how a change in axial

spacing can affect the trajectory of the wake vortices through the rotor passage. The spacing change was chosen such that the rotor shock strength at the vane trailing edge plane (which set the strength of the shed vortices) differed by less than 2%. The difference in Mach number at the vane trailing edge plane between the two configurations was 0.01 (the Mach number is 1.05 in $close_{2D}$ and 1.06 in far_{2D}). The number of grid points for both configurations is given in Table 6.1. The same number of grid points was maintained for the $close_{2D}$ and far_{2D} vanes, but the distance between grid points in the axial direction was decreased for $close_{2D}$. Since the mesh in the far_{2D} was already sized to capture the important flow features in the axial gap region, the finer mesh in $close_{2D}$ will also capture the important flow features.

Table 6.1: Number of grid points in axial, radial and pitch-wise directions for the two-dimensional calculations.

Blade row	Axial	Radial	Pitch-wise
Rotor	189	2	81
Vane $close_{2D}$	230	2	61
Vane far_{2D}	230	2	61

A comparison of performance between far_{2D} and $close_{2D}$ was made at the same mass flow. The stagnation pressure ratio and stagnation temperature rise at the mixed-out conditions are given in Table 6.2, while the efficiencies at the rotor exit and far downstream are given in Table 6.3. All are lower for $close_{2D}$ compared to far_{2D}. $Close_{2D}$ exhibits 3% less work than far_{2D} and has a 1.7% lower stagnation pressure ratio. The difference in efficiency at the rotor exit is 0.01 points (lower in $close_{2D}$ than far_{2D}), which is not of interest, but at the far downstream mixed-out state, the difference in efficiency is greater, with $close_{2D}$ 0.3 points lower than far_{2D}. The majority of the difference in entropy generation thus occurs downstream of the rotor trailing edge (see discussion in the following)

Table 6.2: Mass flow rate, mass-averaged total temperature rise, and mass-averaged total pressure from two-dimensional calculations for far_{2D} and $close_{2D}$ configurations. Values are time-averaged at downstream infinity.

Spacing	Mass flow (kg/s)	Mass-average T_t rise	Mass-average p_t ratio
$Close_{2D}$	1148.47	0.187	1.739
Far_{2D}	1149.54	0.193	1.772

Table 6.3: Efficiency η for far_{2D} and $close_{2D}$ spacing configurations at the rotor exit and at downstream infinity.

Spacing	Rotor Exit	Downstream infinity
$Close_{2D}$	0.9405	0.9205
Far_{2D}	0.9406	0.9235
Difference	0.0001	0.0030

The configurations examined and assessed, referred to as "close$_{2D}$" and "far$_{2D}$," had axial blade row spacings of 0.81 and 0.91 of the chord length, respectively. The value of $B3$ for close$_{2D}$ is 16.7 and for far$_{2D}$ is 18.8. At the same vane inlet corrected mass flow, close$_{2D}$ experiences a 3% decrease in work input and a 1.7% lower stagnation pressure ratio compared to far$_{2D}$. The efficiency at the rotor trailing edge is 0.01 points lower in close$_{2D}$ compared to far$_{2D}$, however, close$_{2D}$ is 0.3 points lower far downstream.

These changes can be linked to the different vortex trajectories within the rotor passages for the two configurations, as pictured in the entropy contours of Figure 6.3. For far$_{2D}$, a clockwise vortex enters the mid-passage of the rotor, while a counter-clockwise vortex intersects the rotor leading edge and remains near the blade. For close$_{2D}$, both vortices move through the rotor but are away from the blades.

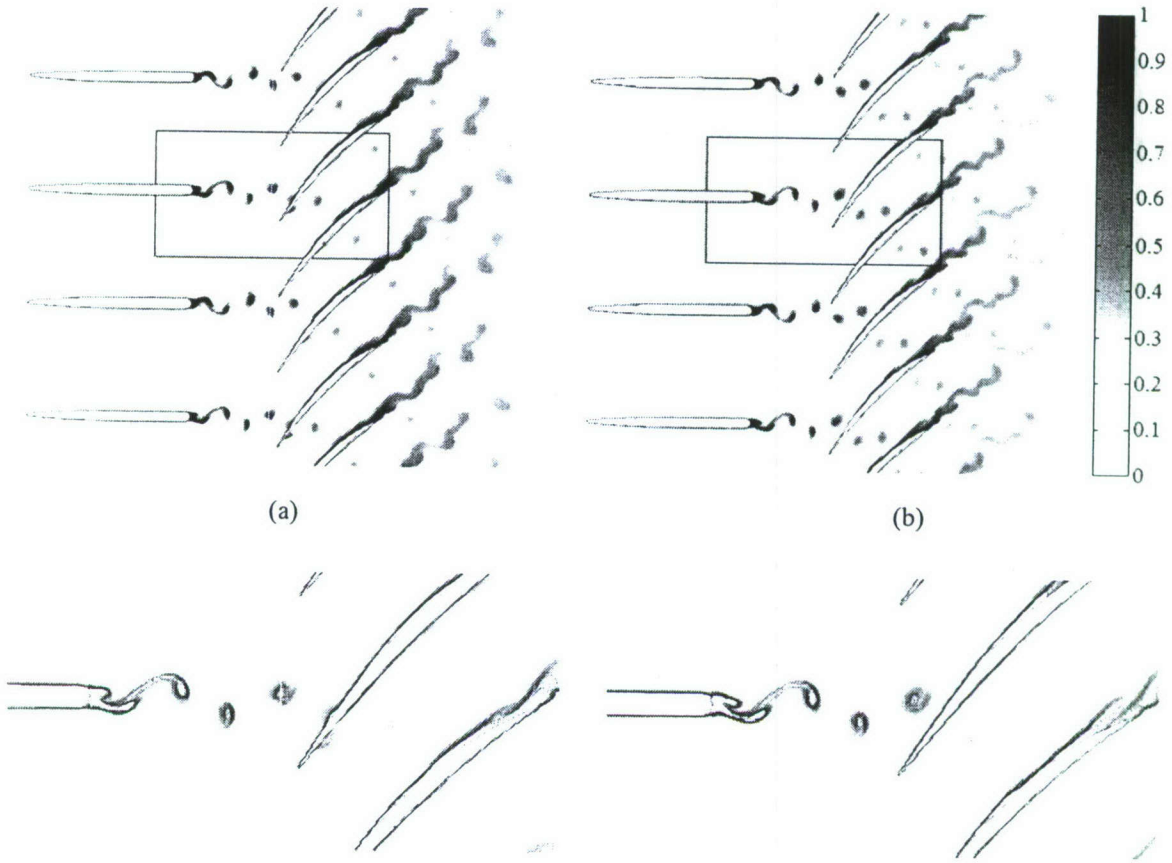

Figure 6.3: Entropy contours for (a) far$_{2D}$ and (b) close$_{2D}$. Comparison of both configurations shows different relative locations of vortices in the rotor blade passages. All plots are of the same scale. The lower contour plots correspond to the boxed regions in the upper plots, and have 20 evenly-spaced intervals.

Time-averaged entropy contours in the rotor frame of reference are given in Figure 6.4. The largest values of the time-averaged entropy are along the blade surfaces, representing the rotor boundary layers. Away from the blades, streaks of smaller time-averaged

entropy than that in the boundary layers delineate the path of the vortices, made clearer by dashed lines. A single streak of entropy is visible in far_{2D}, while two streaks are seen at a different relative location to the blades in $close_{2D}$.

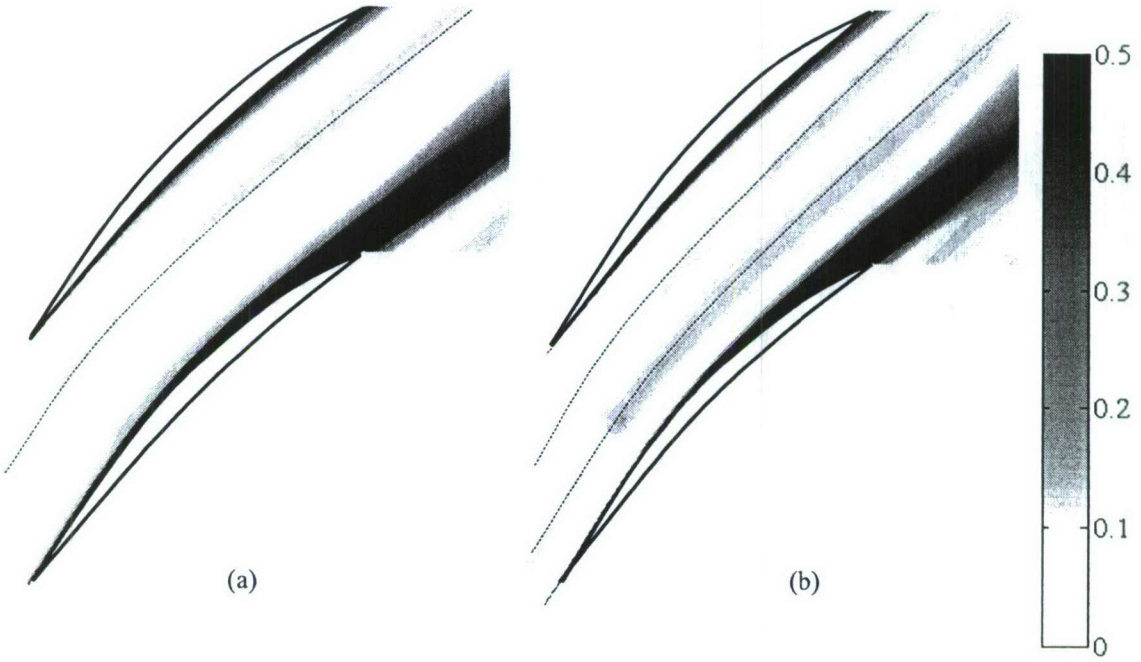

Figure 6.4: Time-averaged entropy contours within the rotor passage for (a) far_{2D} and (b) $close_{2D}$. Streaks of entropy within the passage delineate the path taken by the vortices. Two streaks are visible in $close_{2D}$, while only one is seen in far_{2D} because the other vortex is located within the rotor boundary layer.

6.3 Vortex Strength and Size in Vane-Rotor Gap Region

In this section, the performance differences measured between the two configurations will be shown to be due to *changes in the vortex trajectory*, and *not* to changes in vortex strength or size that occur with spacing. The term vortex strength refers to the net circulation, and vortex size refers to the vortex physical extent (such as the equivalent radius). The vortex size at the rotor leading edge plane varies with spacing because of the different lengths over which the vortices can diffuse before they enter the rotor. If the vortex strength or size is different at the rotor leading edge plane in the two configurations, there can be differences in entropy generation processes not associated with a change in vortex trajectory. These entropy generation processes include different levels of viscous dissipation, and different interactions with the rotor shock and boundary layer (e.g. a vortex of larger circulation and size can influence the velocity field more strongly). It is shown below that differences in vortex circulation and size are negligible between the two configurations.

The difference in vortex strength is first assessed by calculating the vortex circulation for clockwise rotating vortices at the rotor leading edge in $close_{2D}$ and far_{2D}. For far_{2D}, the clockwise vortex remains within the rotor core flow (away from the boundary layers),

while the counter-clockwise vortex travels along the blade surface. For $close_{2D}$, both counter-rotating vortices remain within the core flow.

The circulation is:

$$\Gamma = \int \omega dA, \tag{6.4}$$

where the vorticity ω is computed from velocity gradients using a centered-difference scheme. The normalized circulation is given in Table 6.4, which shows 2.8% difference between far_{2D} and $close_{2D}$. The difference in circulation should be the same for the counter-clockwise vortices since there is a small net loading on the upstream vane row (the difference in the time-averaged flow angle at the vane trailing edge between the two configurations was measured to be 0.2 degrees). Measuring the circulation for the counter-clockwise rotating vortex at the rotor inlet is not possible for the far_{2D} configuration because it is intersected by the rotor blade.

Table 6.4: Circulation for the clockwise vortex at the rotor trailing edge.

	$\Gamma/(Tip\ Speed * c_x)$
Far_{2D}	0.1598
$Close_{2D}$	0.1517
% difference $Far_{2D} - Close_{2D}$	2.8%

To assess the difference in vortex size, a vorticity-weighted radius is used, defined as:

$$\bar{r}^{\omega} = \frac{\int r\omega dA}{\int \omega dA}, \tag{6.5}$$

where the radial coordinate r is measured from the location of maximum vorticity. The value of $\bar{r}^{\omega}$ represents a vortex of constant vorticity and radius $\bar{r}^{\omega}$, outside which the vorticity is zero, as in Figure 6.5.

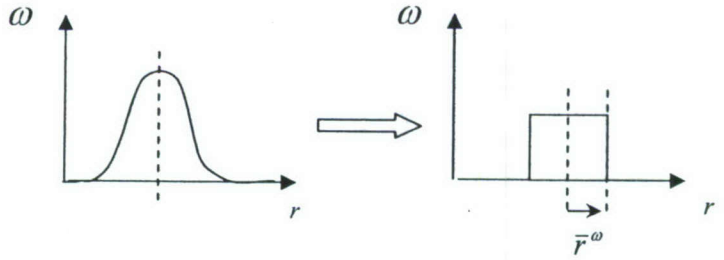

Figure 6.5: Vortex equivalent radius, (a) distribution of vorticity as a function of radius, and (b) equivalent radius to describe the distribution of vorticity depicted in (a).

Table 6.5 gives $\bar{r}^{\omega}$ for the clockwise vortices described by Table 6.4. The difference in radii for the two configurations is 10.4%.

Table 6.5: Circulation-weighted radii for the clockwise vortex at the rotor trailing edge.

	$\bar{r}^{\omega}/pitch$
Far_{2D}	0.0625
$Close_{2D}$	0.0566
% difference $Far_{2D} - Close_{2D}$	10.4%

The small effect of differences in the circulation and size of the shed vortices on performance differences between far_{2D} and $close_{2D}$ are confirmed by comparing the non-uniformity in the velocity field at the rotor leading edge. A measure of the non-uniformity at any given plane is the quantity:

$$\frac{1}{2}\rho u'^2, \tag{6.6}$$

where u'^2 is defined as:

$$u'^2 = (u_x - \bar{u}_x)^2 + (u_y - \bar{u}_y)^2. \tag{6.7}$$

The overbar represents the time- and pitch-wise area- average of the velocity component. With no pressure variations within the flow, the quantity in (6.6) represents the potential for stagnation pressure loss in an incompressible flow, as derived in Appendix A. In the case of interest, there are pitch-wise non-uniformities in the velocity due to the rotor pressure field, but the pressure field is assumed to change the non-uniformity metric by the same magnitude in both configurations.

The non-uniformity metric, averaged over the pitch and in time, and non-dimensionalized by the dynamic head at the inlet is:

$$\frac{\overline{\frac{1}{2}\rho u'^2}}{p_{t,inlet} - p_{inlet}} = \frac{\frac{1}{\tau}\frac{1}{A_{total}}\int\left[\int\frac{1}{2}\rho u'^2 dA\right]dt}{p_{t,inlet} - p_{inlet}}. \tag{6.8}$$

The quantity in (6.8) is plotted in Figure 6.6 as a function of axial location. In Figure 6.6(a), the difference in the non-uniformity metric differs by 0.2% between the two configurations at the rotor leading edge. In Figure 6.6(b), the curve for $close_{2D}$ is shifted to the right so that the vanes in both configurations are aligned at the same axial location, as opposed to the rotor blades being aligned in Figure 6.6(a). It can be seen that the non-uniformity metric follows similar trends up to the rotor leading edge for both configurations. However, the trend within the rotor and downstream differs between the two configurations, indicating different flow fields within the rotor. The differences within the rotor are due to the different vortex trajectories, since this is the only differing

flow feature entering the rotor. At the rotor trailing edge, the difference in the non-uniformity metric between configurations is 23%, much greater than at the leading edge. In summary, the rotor is subjected to a similar non-uniformity at the leading edge in both configurations.

With a similar non-uniformity ahead of the rotor, the performance differences between far_{2D} and $close_{2D}$ can be linked to how the vortices are processed within the rotor, due to their relative respective trajectories. This is discussed in the next section.

6.4 Rotor Response to a Change in Vortex Trajectory

The rotor behavior due to a change in vortex trajectory is first assessed in terms of the difference in work input and efficiency. Although there is a lower work input in $close_{2D}$ compared to far_{2D}, the efficiency at the rotor trailing edge is similar for the two cases. For $close_{2D}$, the lower work input (lower total temperature rise), is accompanied by a lower entropy rise with respect to far upstream. However, the difference in entropy generation between the two configurations does not occur within the rotor. Instead, more entropy is generated in far_{2D} from the inlet of the domain to the rotor leading edge plane due to higher shock losses from a higher operating back pressure. (Although there are shocks of different strengths in both configurations, the vortices are unaffected by any possible interactions with them, as evidenced by similar values of the non-uniformity metric at the rotor leading edge plane, as in Section 6.3).

The overall entropy rise within the rotor differs by 0.6% between far_{2D} and $close_{2D}$, as seen in time-averaged values in Table 6.6. The entropy increase within the rotor is calculated inside and outside the boundary layer, i.e. the core flow which includes the shock waves, using the computational dissipation described in Section (5.0). For control volumes encompassing these two regions, the reversible heat transfers across the surface are negligible compared to the irreversible viscous and thermal dissipation within the volume, and the integration of the computational dissipation is therefore equal to the entropy generated. The distribution of entropy generation within the rotor passage in both configurations is different, because there are two vortices in the core flow for $close_{2D}$, and one vortex in the core flow in far_{2D}. As seen in Table 6.6, there is a 0.4% difference in the entropy generated within the boundary layer control volume, and 0.9% difference in the core flow. The shock losses (also given in the table) are found to be higher in far_{2D} than $close_{2D}$ by 6.8%. In summary, the overall entropy rise in the rotor for both configurations is similar because there are higher shock losses in far_{2D} but less mixing losses (from one vortex in the core flow for far_{2D}, versus two vortices in $close_{2D}$).

Note that the difference in shock losses are of the same magnitude as the differences in losses from the vortices in the core flow, which is not the case for the three-dimensional configurations described in Section (5.0). The reason for this is that the difference in blade row spacing for the three-dimensional configurations is six times larger than the difference in the two-dimensional configurations. Thus, the difference in the strength of the vortices is also much greater, and a larger difference in entropy generation from the vortices compared to the difference in shock losses.

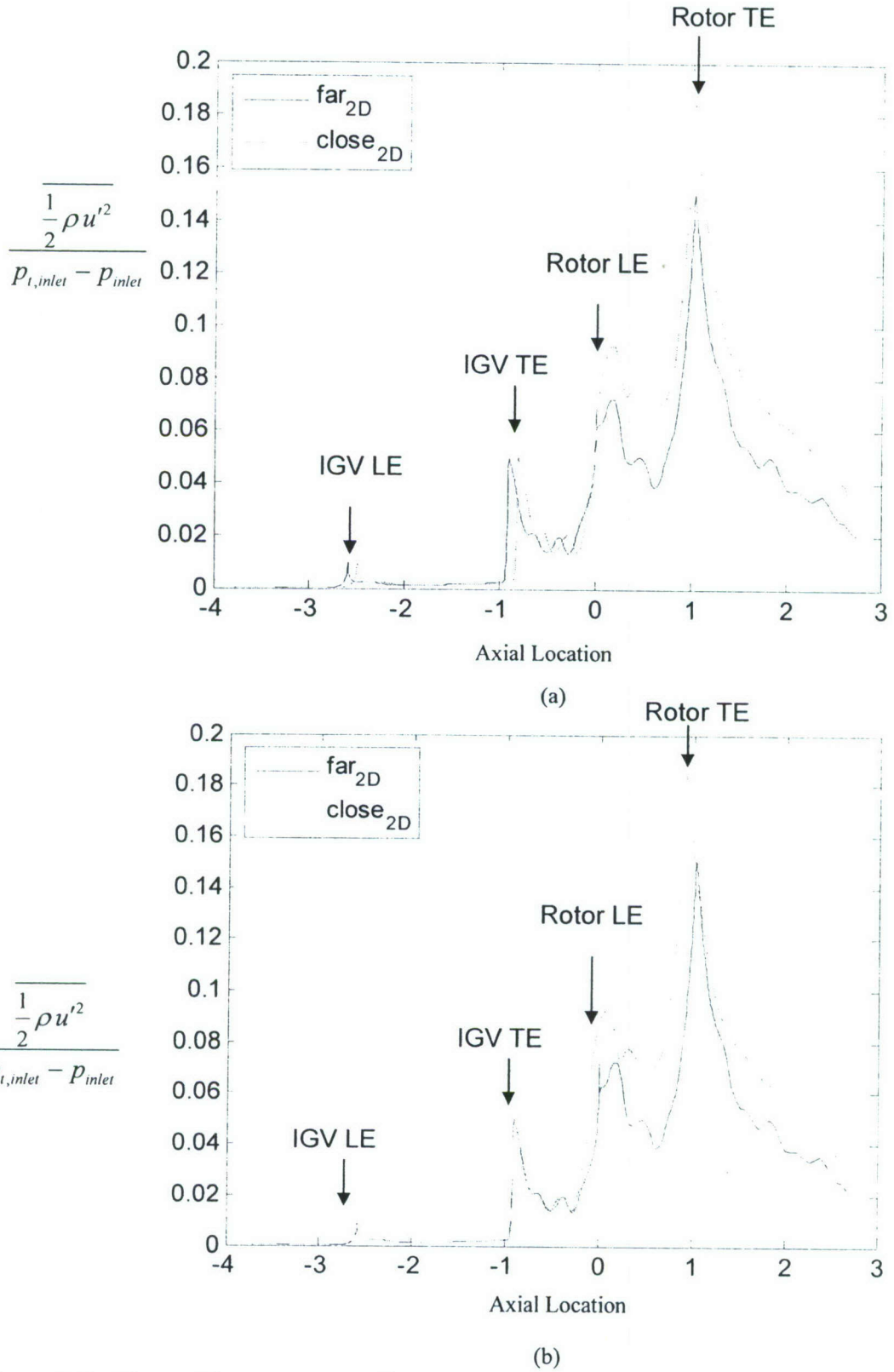

Figure 6.6: Non-uniformity metric of equation 6.8 as a function of axial position with (a) the rotor blades in both configurations at the same axial location, (b) the vanes at the same axial location.

Table 6.6: Time-averaged entropy generation in specified control volumes within rotor.

	Overall	Boundary layer	Core flow	Rotor shock
Far_{2D}	0.0925	0.0625	0.0300	0.0521
$Close_{2D}$	0.0931	0.0628	0.0303	0.0488
$Close_{2D}$ - Far_{2D} % difference	0.6%	0.4%	0.9%	-6.8%

While the entropy generation within the rotor is similar between the two configurations, the different vortex trajectories within the rotor cause the entropy generation downstream of the rotor to be different, leading to a 0.3 point difference in efficiency far downstream. The differences in the flow field at the rotor trailing edge plane are the number of vortices in the core flow and the sizes of the boundary layers. The effect of the different boundary layers on the difference in entropy generation downstream of the rotor for the two configurations is now assessed.
In Figure 6.7, the red color marks areas where the $close_{2D}$ boundary layer is larger than the far_{2D} boundary layer, and the blue color marks where the far_{2D} boundary layer is larger. The boundary layer is defined as the location with the computational dissipation (based on the expression in equation (5.4)) at least two orders of magnitude higher than the core flow.

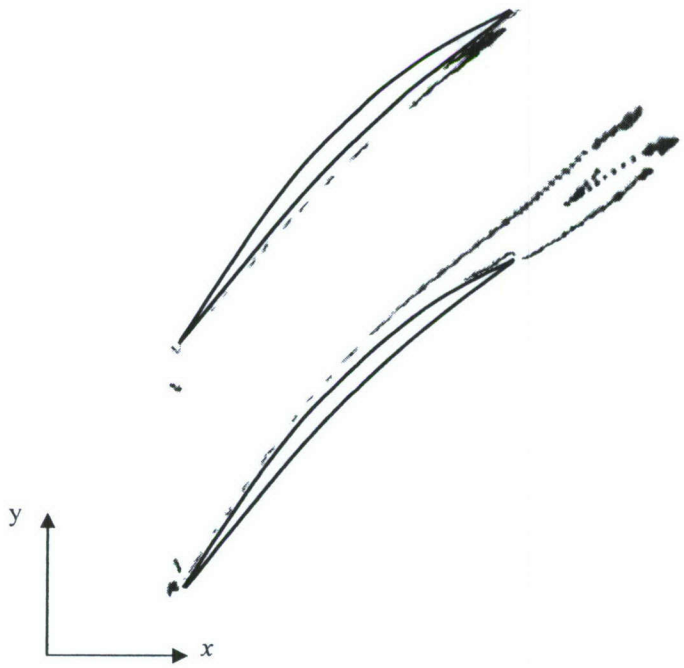

Figure 6.7: Differences in boundary layers between far_{2D} and $close_{2D}$. Red regions: $close_{2D} > far_{2D}$, Blue regions: $far_{2D} > close_{2D}$.

Three boundary layer characteristic quantities are calculated at the rotor trailing edge, for both pressure and suction sides. These are the displacement thickness

$$\delta^* = \int_0^{y_E} \left(1 - \frac{u_x}{u_E}\right) dy_E \,, \tag{6.9}$$

the momentum thickness

$$\theta = \int_0^{y_E} \left(1 - \frac{u_x}{u_E}\right) \frac{\rho u_x}{\rho_E u_E} dy_E \,, \tag{6.10}$$

and the energy thickness

$$\theta^* = \int_0^{y_E} \left(1 - \frac{u_x^2}{u_E^2}\right) \frac{\rho u_x}{\rho_E u_E} dy_E \,. \tag{6.11}$$

In these, the subscript E represents the free stream condition. The displacement thickness and momentum thickness are larger in $close_{2D}$ than far_{2D} by 13% and 3% respectively. The energy thickness is greater in far_{2D} than $close_{2D}$ by 4%. A larger boundary layer in $close_{2D}$ is consistent with a reduced work input compared to far_{2D} (see Section 7 below)

The entropy generation from the mixing of the boundary layers from the rotor trailing edge plane to far downstream is assessed to determine its contribution to the total entropy generated in the same region in both configurations. The entropy rise from the boundary layers has been estimated assuming a uniform core flow, and solving the two-dimensional conservations equations using the quantities calculated from Equation (6.9)-(6.11). The procedure is outlined in Appendix B. The overall entropy rise generated from the rotor exit to far downstream, and the entropy rise from the mixing of the boundary layers alone, are given in Table 6.7. The difference in the boundary layer entropy rise accounts for 40% of the difference in the entropy rise between $close_{2D}$ and far_{2D}. Therefore, the effect of vortex trajectory on the entropy generation downstream of the rotor is at least partly due to its effect on the rotor boundary layers. Moreover, there was less entropy generated downstream of the rotor when one vortex was located near the blade surface, which makes the vortex trajectory in far_{2D} favorable to that in $close_{2D}$.

Table 6.7: Entropy rise from rotor trailing edge to far downstream.

	Overall	Boundary Layer
$Close_{2D}$	0.0568	0.0233
Far_{2D}	0.0489	0.0203
Difference ($Close_{2D}$-Far_{2D})	0.0078	0.0030

The remaining difference in the entropy rise measured far downstream must be due to the mixing and diffusion to a final uniform state of two vortices in the core flow for $close_{2D}$ versus one vortex for far_{2D}. The difficulty in measuring the entropy generation from the vortices directly from the 2D simulations is isolating them from the rest of the flow field. Downstream of the rotor trailing edge, the rotor boundary layer and vortices mix together so that isolating the vortex at each instant in time while following it downstream becomes difficult. Further, a defining characteristic associated with the vortices was not obvious, since these characteristics were also associated with other parts of the flow field (for example, using vorticity to mark the vortices would also capture regions of the rotor

boundary layer). Marking the fluid particles associated with the vortices from their inception at the vane trailing edge is also difficult. Future work is thus suggested to conclusively demonstrate that the mixing of the vortices in the core flow accounts for the remaining difference in entropy generation.

6.5 Results of Zachcial and Nurnberger[6]

Before we conclude this section, we should note that Zachcial and Nurnberger (2003) also examined the effect of a variation in axial blade row spacing. They used two-dimensional unsteady calculations for a transonic stator/rotor combination for three different axial spacings (19.9%, 24.2% and 28.4% of the rotor chord length) operating at the same back pressure. An improvement in efficiency was found with decreased spacing, opposite to the results in Figure 3.2 and to the work by Gorrell (2001), Gorrell et al. (2003). No discussion concerning this discrepancy was given by Zachcial and Nurnberger (2003). The improved performance was due to a reduction in boundary layer separation within the rotor, leading to lower blade profile losses. Their observed trend in efficiency coincided with a change in the vortex trajectory within the rotor passage as blade row spacing is changed. However, the connection between a change in the vortex trajectory and the reduction in blade profile losses was inferred from the pitch-wise distribution of entropy at location 1.5 rotor pitches downstream of the rotor, which is not as accurate as direct examination, as it is done in the present work, of the location where entropy is created.

Zachcial and Nurnburger (2003) carried out an extensive parameter study to determine the various parameters that affect the vortex pattern within the rotor, including changes in rotational speed, axial gap and stator pitch. It was found that a change in the rotational speed and the axial gap changed the relative location of the vortex within the rotor, while a change in the stator pitch has no effect. This is consistent with the results presented in Section (6.0) this report.

Zachcial and Nurnberger determined that as axial blade row spacing increased, a minimum value of the efficiency is attained before reaching a constant value. The reason a minimum efficiency is obtained was not addressed. Based on the results of this report, it is postulated that the minimum can be explained by two competing effects, namely the change in vortex circulation and the relative location of vortices in the rotor with changes in spacing. A decrease in spacing can result in an increase in the entropy contained in the vortices and a decrease in efficiency, but a change in the relative location of the vortex within the rotor may give an increase in efficiency. This motivates the study of the effect of the vortex trajectory within the rotor, as its impact may lead to an optimal spacing, and is also an example of how unsteady flow events drive time-average changes that are of engineering significance.

---

[6] In a technical discussion on the impact of vortex trajectory within rotor on its performance, Gorrell (2006) referred the investigators of this research program to the work of Zachcial et al. (2003) on influence of vane-rotor spacing on compressor operating points.

6.6 A Summary on Impact of Vortex Trajectory on Rotor Performance

Two configurations are studied which have an axial spacing between the vane and rotor that differ by 11%. The change in blade row spacing results in two different vortex trajectories within the rotor. In one, there are two vortices in the passage core flow. In the other, one vortex is within the passage core flow, and the other travels along the surface of the blade. It is found that the configuration with two vortices in the core flow has a lower work input (by 3%) and lower efficiency (by up to 0.3 point). The difference in the rotor performance is attributed to the difference in vortex trajectory through arguments that the flow non-uniformity ahead of the rotor is similar for both spacings. Roughly 40% of the difference in the downstream efficiency is attributed to a difference in the boundary layer at the rotor trailing edge.

7.0 Flow Modeling on Effect of Vortex Trajectory within Rotor

We showed and described in Section 6 that the performance of the rotor is affected by the specific trajectory of IGV discrete vortices within the rotor blade passage. Figure 6.3(a) and 6.3(b) show two entropy contour plots of IGV wake discrete vortices entering and traversing through the rotor row. The rotor geometry and the time- and pitchwise-averaged flow field entering the rotor blade-row are the same for both the situations shown in Figure 6.3. However, the path of the wake vortices in Figure 6.3(a) is distinctly different from that of the wake vortices in Figure 6.3(b). This difference in the vortex trajectories results in a change in the performance of the rotor; at the same corrected mass flow, the $Close_{2D}$ configuration in Figure 6.3(b) had a 3% reduction in work input and up to a 0.3 point drop in efficiency compared to that of the Far_{2D} configuration in Figure 6.3(a).

The change in the positioning of the wake vortices relative to the rotor can be viewed as a change in the phase between the wake and the rotor blade passing. In this section, this flow feature will be referred to as wake phasing (in contrast to clocking of the blade-rows) and characterized by the B3 parameter introduced in Section 6 above; a change in the B3 parameter thus corresponds to a change in wake phasing. It can be shown that changes in the phase between the wake and the rotor blade passing can be caused by a change in any of the following parameters: inter-bladerow spacing (L), wheel speed (Ω), convective velocity (U), rotor pitch ($2\pi/nblades$), and shock angle (θ).

A steady-state flow model is presented in this section for explaining and estimating the change in compressor performance resulting from a change in the wake phasing. A series of two-dimensional computational experiments are then carried out to assess the model. The goal here are twofold: one is to determine how and why the rotor performance changes when the wake phasing is changed (this includes being able to explain which fluid mechanisms are important to the phenomenon, as well as producing a simplified model which only considers the key mechanisms), and the other is to test the ability of the proposed steady-state model to estimate and explain the change in performance with changes in wake phasing.

7.1Rotor Response to Pitchwise Shift in Inlet Total Pressure Non-uniformity

The response of rotor performance to changes in wake phasing can be more directly addressed by examining the flow field in the rotor relative frame. On a time-average basis, the unsteady shedding of the wake vortices from the upstream IGV appears as stratification in (relative) total pressure across the pitch of the rotor inlet in the rotor frame. Thus any change in the wake phasing would manifest itself as a pitchwise shift of (relative) total pressure stratification. The entropy contours in Figure 6.3(a) and 6.3(b) reflect the difference in phasing between the wake and the rotor blade passing. On the time-average basis (in the rotor reference frame), this corresponds to a pitchwise shift in the entropy non-uniformity distribution shown in Figure 6.4.

The above observation and interpretation strongly suggests that "assessing the rotor performance response to changes in wake phasing" becomes one of "determining performance response of an isolated rotor to changes in the pitchwise location of inlet (relative) total pressure non-uniformity". This in essence provides the technical basis for formulating a steady-state flow model for assessing the effects of changes in wake phasing on rotor performance.

MSU Turbo was used to implement a series of steady-state two-dimensional computational experiments to quantify the change in rotor performance to variations in the pitchwise locations of total pressure non-uniformity. A schematic of such a steady-state flow situations (in the rotor reference frame) is illustrated in Figure 7.1 for two different pitchwise location of wake (total pressure non-uniformity).

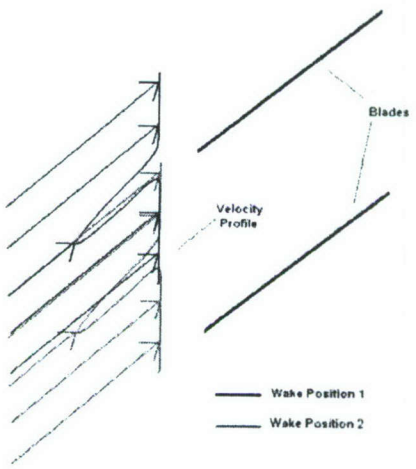

Figure 7.1: A sketch to illustrate wake position as determined by the location where the wake enters the computational domain.

The computed performance characteristics (in terms of total pressure ratio, adiabatic efficiency and total temperature rise normalized by the upstream stagnation temperature) shown in Figure 7.2 correspond to the three different wake positions: wake position 1 (see Figure 7.3(a)), wake position 2, and wake position 3 (see Figure 7.3(b)). The computed relative total pressure distribution corresponding to inlet wake position 1 is

shown in Figure 7.3(a) while that corresponding to inlet wake position 3 is shown in Figure 7.3(b). Wake position 1, 2, and 3 are equally spaced apart at the inlet to the computational domain, with the spacing between adjacent wake positions being 1/3 of a rotor pitch. On a qualitative basis one could infer from Figure 7.3 that the rotor performance corresponding to wake position 1 would be better than that corresponding to wake position 3; this is in accord with the computed performance indicated on Figure 7.2. These computed results show the impact of changing the pitchwise location of wake on the rotor performance characteristics. The computed change in performance at design corrected mass flow is in accord with the result presented in Section 6 on the change in rotor performance associated with the change in the IGV wake vortices trajectory in the rotor passage.

Thus while the change in the time average performance of the rotor is a consequence of unsteady IGV-rotor interactions, the effect can be estimated using a steady-state model of the flow in the rotor frame. The unsteady IGV-rotor interactions (in HLHM compressor) manifests, on a time-average basis, as a stratification in (relative) total pressure across the pitch of the rotor inlet in the rotor frame. A change in any design/operating parameter that lead to a change in the characterizing parameter B3 would thus results in a pitchwise shift of (relative) total pressure stratification.

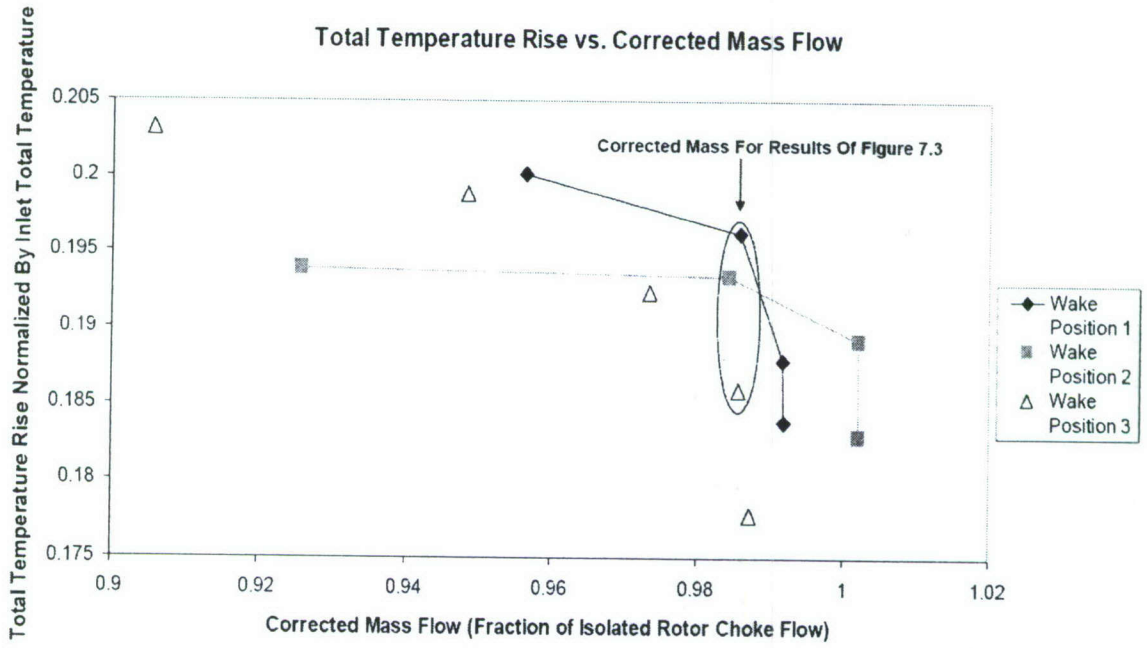

Figure 7.2(a): Computed normalized temperature rise across rotor at various corrected mass flow for three different pitchwise stratifications in relative total pressure.

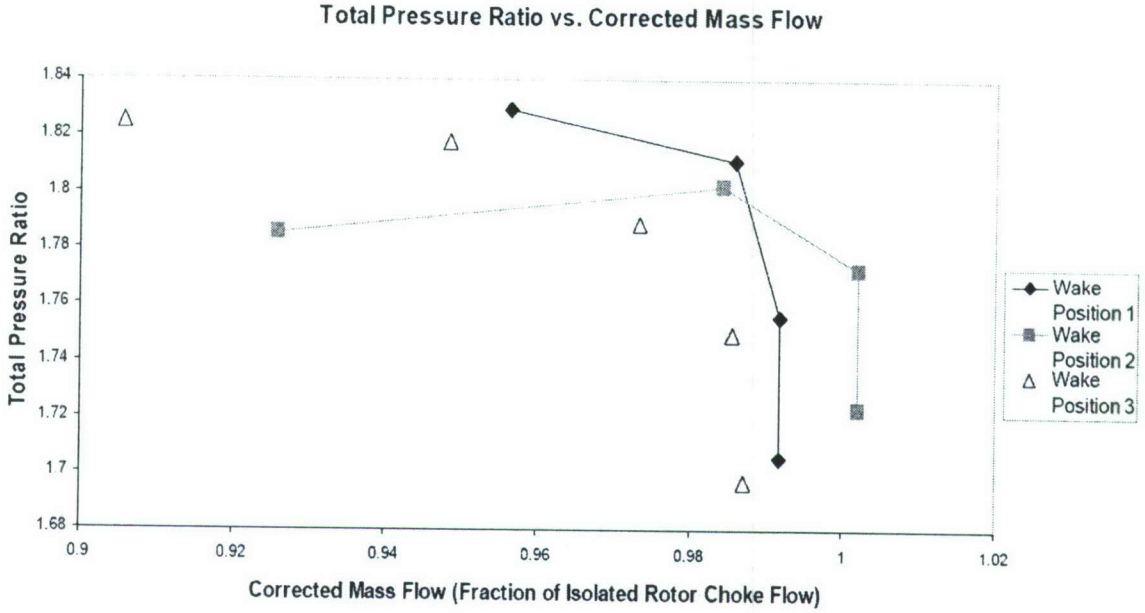

Figure 7.2(b): Computed total pressure ratio across rotor at various corrected mass flow for three different pitchwise stratifications in relative total pressure.

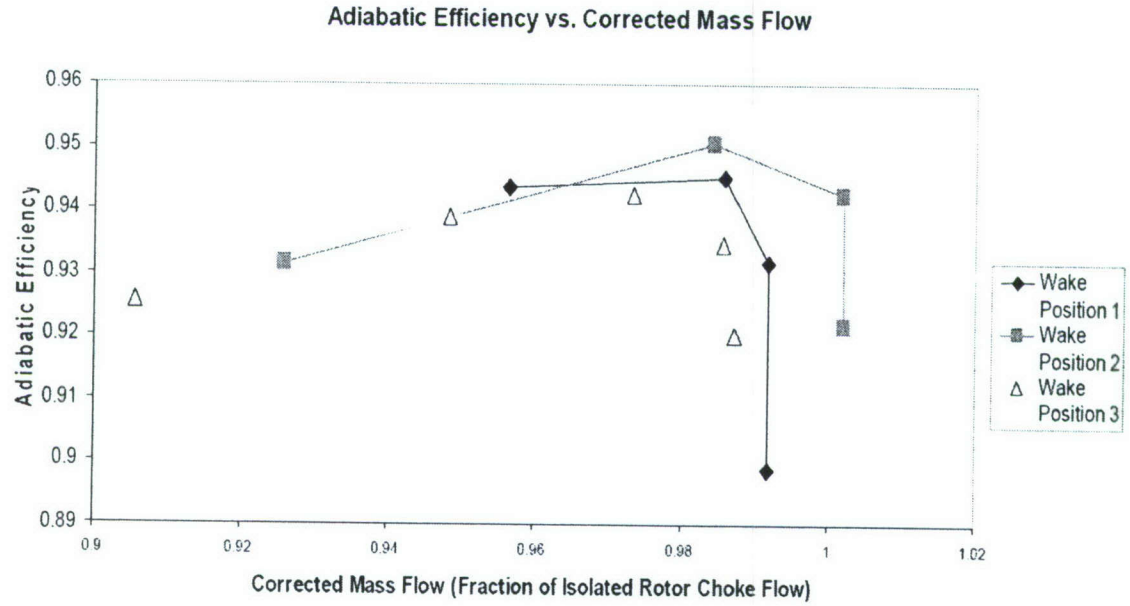

Figure 7.2(c): Computed adiabatic efficiency for rotor at various corrected mass flow for three different pitchwise stratifications in relative total pressure.

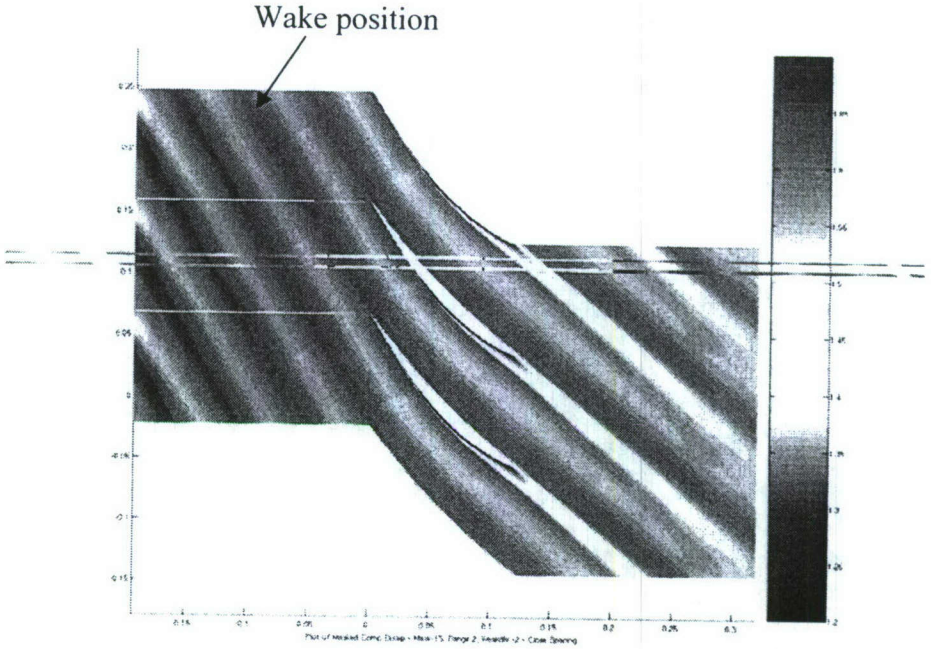

(a) Relative total pressure distribution corresponding to wake position 1

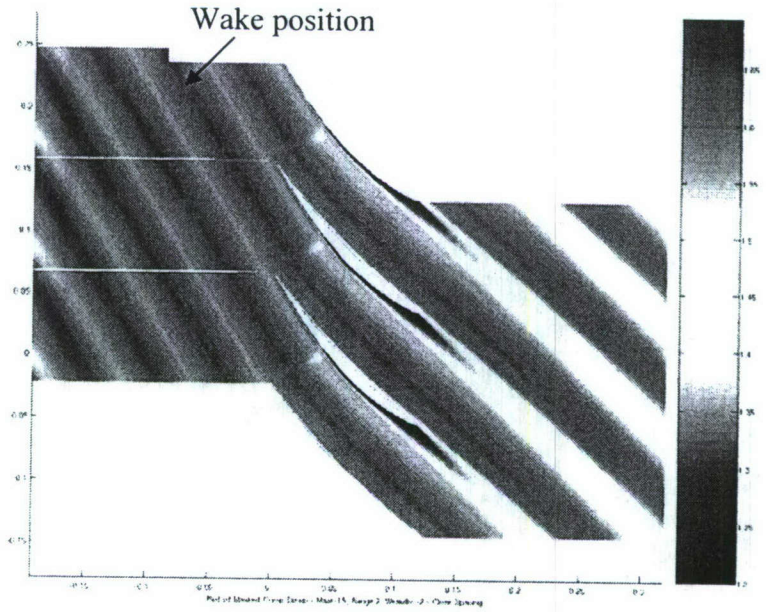

(b) Relative total pressure distribution corresponding to wake position 3

Figure 7.3: Relative total pressure distribution from two-dimensional steady state computations (at corrected mass flow indicated on Figure 7.2(a)) based on MSU Turbo corresponding to two different inlet wake position 1 and 3; the difference between maximum and minimum of the relative total pressure at the inlet is 0.18 relative inlet dynamic head (the contours are relative total pressure non-dimensionalized by atmospheric pressure).

7.2 Analogy with Diffuser Response to Wake and Jet Inlet Velocity Profile

The flow diffusion with accompanying pressure rise in a compressor blade passage is similar to that in a diffuser (Wisler, 1998). The analogy between compressor blade passage and diffuser has been utilized to develop useful correlative criteria for stalling pressure capability in compressor (Koch, 1981). In this section we present the use of the flow in a two-dimensional diffuser subjected to a wake and jet to provide a physical context explaining the response of the rotor performance to the discrete wakes discussed in Section (7.1).

Wolf and Johnston (1969) examined the behavior of a diffuser with a non-uniform core velocity at the inlet; the key aspects of which can be illustrated through comparison of the behavior of diffusers that operate with the two non-uniform inlet flows shown in Figure 7.4. The "jet" profile has a region of high velocity in the center of the channel and low velocity near the walls, whereas the "wake" profile has the opposite. Inlet boundary layer blockage for the two profiles is the same. In the context of rotor performance response to discrete wakes, the jet and wake profile can be view as reflecting the pitchwise shift in relative total pressure stratification.

Measured pressure rise coefficients by Johnston *et al.* (1969) as a function of diffuser area ratio with jet and wake inlet velocity profiles are shown in Figure 7.5. The diffusers operating with the wake profile have a higher performance than those with the jet profile, because the boundary layers of the high velocity stream are more capable of negotiating a given pressure rise. In the context of rotor performance response, this leads to greater blockage and larger deviation at the exit of the blade row, and consequently a smaller pressure rise, in comparison to that achieved when using the wake inlet profile.

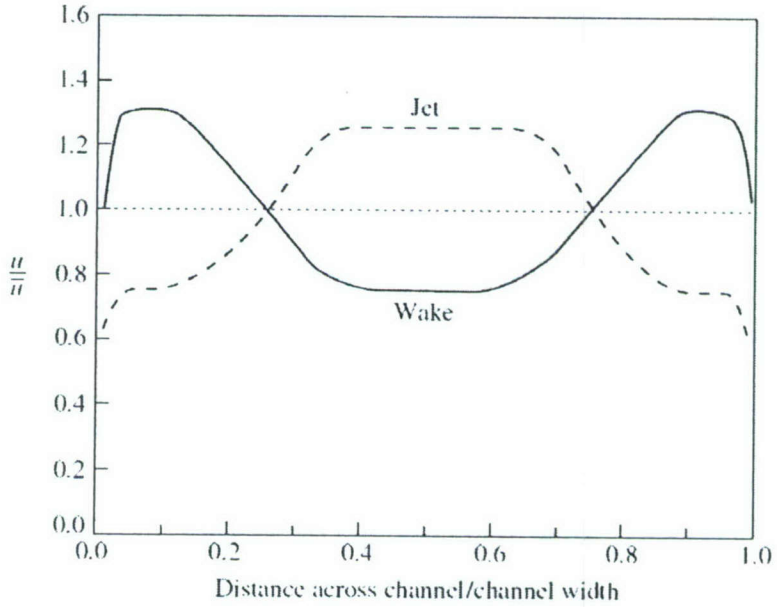

Figure 7.4: Jet and wake inlet velocity profiles for a two-dimensional diffuser (Wolf and Johnston, 1969); $\bar{u}$ denotes the mean velocity.

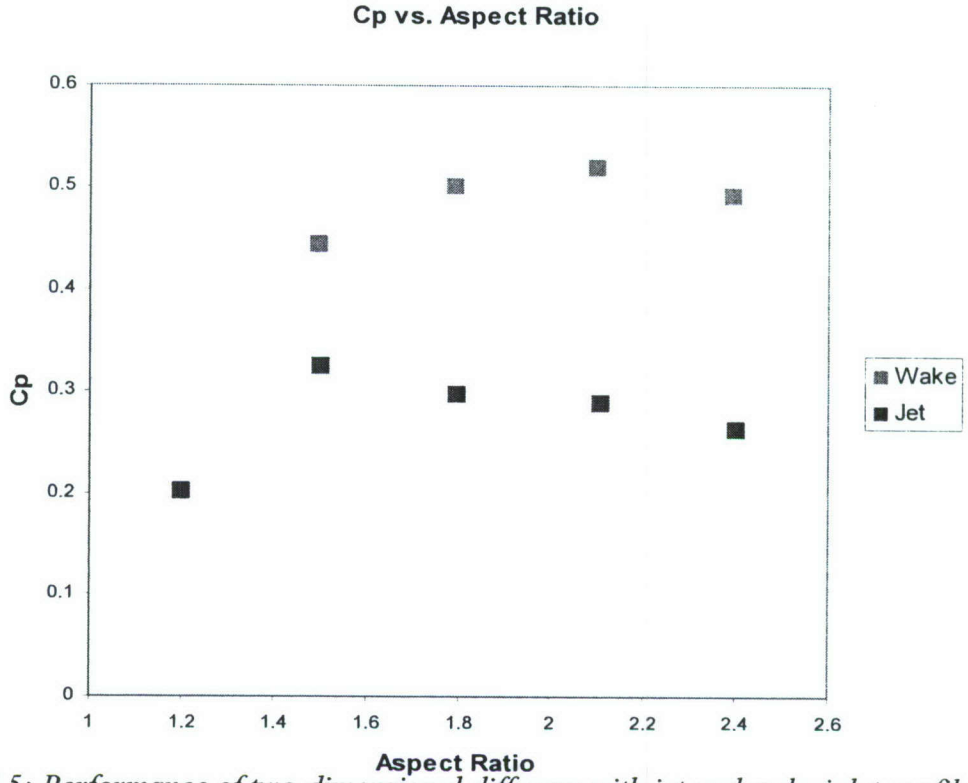

Figure 7.5: Performance of two-dimensional diffusers with jet and wake inlet profiles; inlet boundary layer blockage = 0.012 (Wolf and Johnston, 1969).

We can use the analogy (between diffuser and compressor blade row) to determine the trend in the rotor response and assess if it is in accord with the results presented in Section 6. To do this we first note that the relevant effective flow areas that set the diffusion in compressor blade passage are the areas measured perpendicular to the streamlines at the inlet to and at the exit of blade passage. Thus the pressure rise through an equivalent straight diffuser can be directly related to the tangential force produced by the rotor blade-row, through the following equation:

$$\frac{F_\theta}{\rho u_1 v_1 W_1} = 1 - \left(1 - C_p\right)^{0.5} \frac{\sin\alpha_2}{\sin\alpha_1} \qquad (7.1)$$

In Equation (7.1), F_θ represents the tangential force on the rotor blade, ρ is the fluid density, u_1 is the inlet axial velocity, v_1 is the inlet tangential velocity, W_1 is the blade pitch, α_1 is the inlet flow angle, C_p is the pressure rise coefficient, and α_2 is the exit flow angle.

In the context of rotor blade row, a reduction in C_p translates into a smaller tangential force, and therefore less work done by the rotor. Using Equation (7.1), the reduction in C_p measured by Wolf and Johnston(1969) was shown to be in accord with the reduction in tangential blade force that was computed for the rotor. Furthermore, as was described in Section 6, computations show that the potential for entropy generation at the rotor trailing

edge is also increased (because the rotor blade boundary layer thickness has increased), which results in reduced efficiency.

In the next section we illustrate the utility of this framework of steady-state flow model for providing means of: (1) a more direct (parametric) assessment of rotor performance changes to changes in the pitchwise location of discrete wakes entering the rotor passage; and (2) establishing the scaling of such an effect.

7.3 Scaling of Effect Associated with IGV-Rotor Interactions

The parametric assessment of rotor performance response to changes in the pitchwise location of discrete wakes was carried out using MISES (Drela *et al.* 1998). MISES is a coupled viscous/inviscid Euler method for computing steady flow in a stationary or rotating turbomachinery cascade. In essence it is a streamline-based Euler discretization and a two-equation boundary layer formulation that are coupled through the displacement thickness which are then solved simultaneously using a full Newton method.

A steady, non-uniform total pressure distribution (an example of which is shown in figure 7.6) was specified at the inlet to the computational domain for a stationary blade row. The pitchwise position of the distribution was varied, and the corresponding change in tangential force computed. The change in boundary layer characteristics (in the trailing edge region of blades) accompanying a change in pitchwise shift of the specified non-uniform total pressure distribution is indicated in figure 7.7. When the low total pressure fluid bathes the blades (analogous to the "jet" profile used by Wolf and Johnston(1969)), the suction side boundary layer thickness is relatively larger and thus reduces the ability of the blade row to diffuse the flow somewhat because the effective exit area is reduced. The reduction in exit flow area is due to a combination of increased blockage and increased deviation angle at the trailing edge, a result similar to that observed by Wolf and Johnston (1969) described in Section (7.2).

Calculations of steady flow in a blade-row using MISES as described in the above have been carried out for various pitchwise location and strength of the incoming wakes as well as inlet Mach number. The computed results have been post processed in a manner to elucidate the scaling of the wake phasing effect with inlet relative total pressure non-uniformity and inlet Mach number. The non-dimensional quantities that are appropriate for the scaling discussion are the inlet Mach number, and the parameters described below:

$$\delta F_\theta = \frac{F_\theta - \overline{F_\theta}}{(\overline{P_t}^{MA} - P) \cdot W \cdot c} \qquad (7.2)$$

$$\delta P_t = \frac{\Delta P_t}{\overline{P_t}^{MA} - P} \qquad (7.3)$$

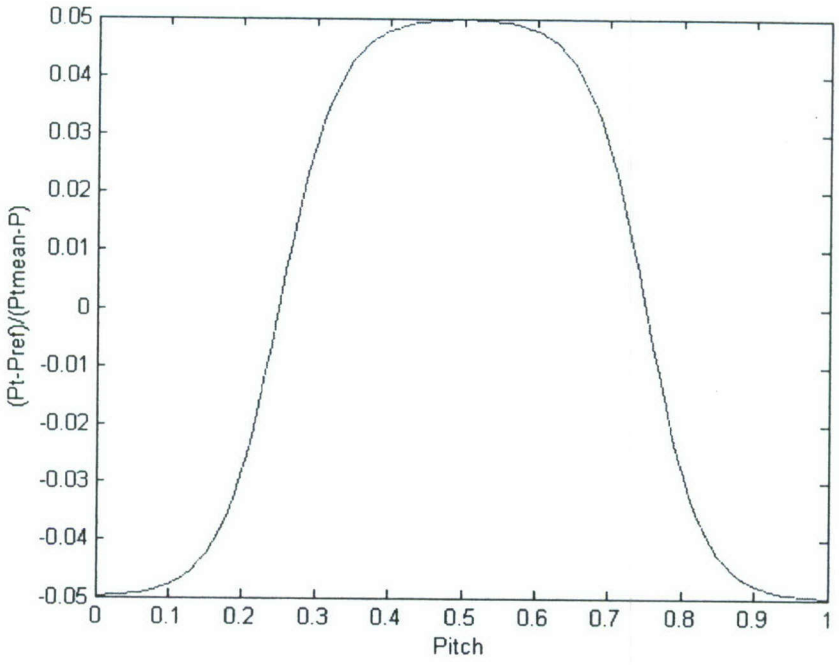

Figure 7.6: An example of the distribution of total pressure that was used for the MISES calculation. The amplitude of the distribution was varied in order to consider various scaling properties, but the general shape of the distribution was kept the same.

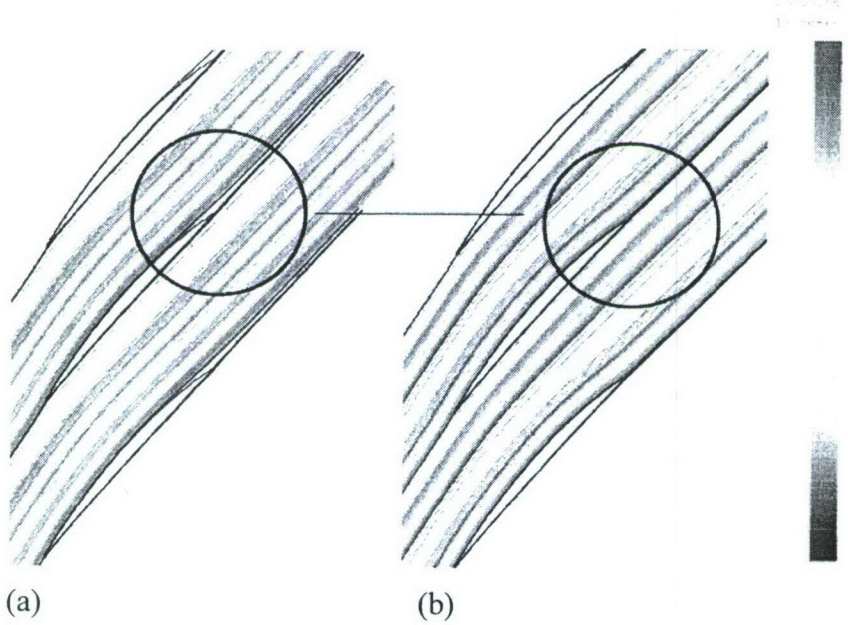

Figure 7.7: Contours of total pressure for 2 different pitchwise positions of inlet total pressure non-uniformity. One should note that in case (a), where the low total pressure fluid bathes the blade, the suction surface boundary layer thickness at the trailing edge is larger than that case (b).

In Equation (7.2), the numerator represents the difference between the tangential force on the blade with non-uniform inlet flow and that for uniform inlet flow. The denominator is a product of the inlet dynamic head, the blade pitch and the blade chord. Equation (7.3) represents the peak to peak difference in inlet total pressure, normalized by the inlet dynamic head.

Figure 7.8 shows the non-dimensional force δF_θ as a function of the pitchwise position of the total pressure non-uniformity δP_t for various inlet Mach number M; the non-dimensional inlet total pressure non-uniformity was kept the same. The Prandtl-Glauert Rule has been used to correct the δF_θ values for compressibility. One can see that in the non-dimensional context presented here, the results are independent of the inlet Mach number M.

Figure 7.9 shows the non-dimensional force δF_θ normalized by the specified inlet total pressure non-uniformity as a function of the pitchwise position of the total pressure non-uniformity δP_t; the magnitude of the inlet total pressure non-uniformity is varied while the inlet Mach number is held fixed. Since the computed data points collapse onto a single curve, one infers that the change in the non-dimensional force δF_θ is directly proportional to the magnitude of the inlet total pressure non-uniformity.

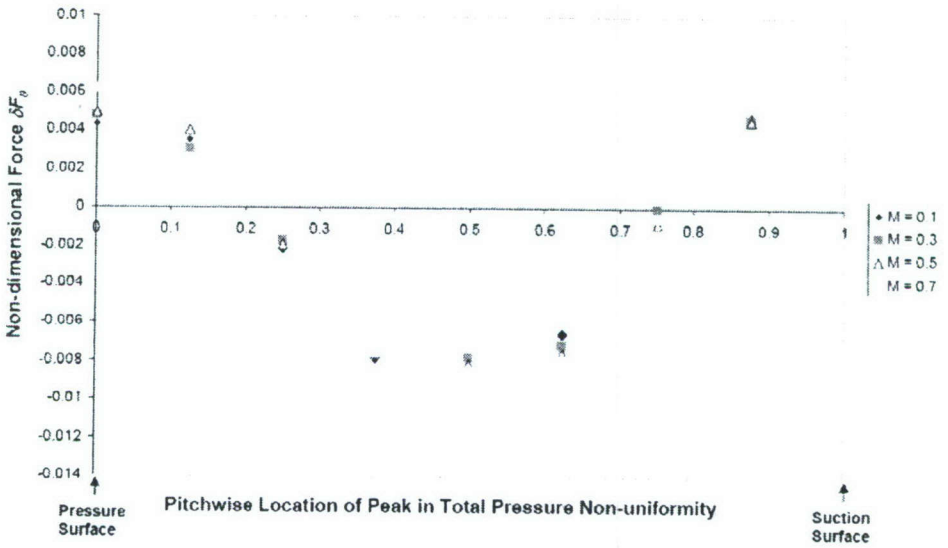

Figure 7.8: Non-dimensional force δF_θ (Equation 7.2) as a function of pitchwise location of inlet total pressure non-uniformity for various inlet Mach number M with the specified non-dimensional inlet total pressure non-uniformity held fixed.

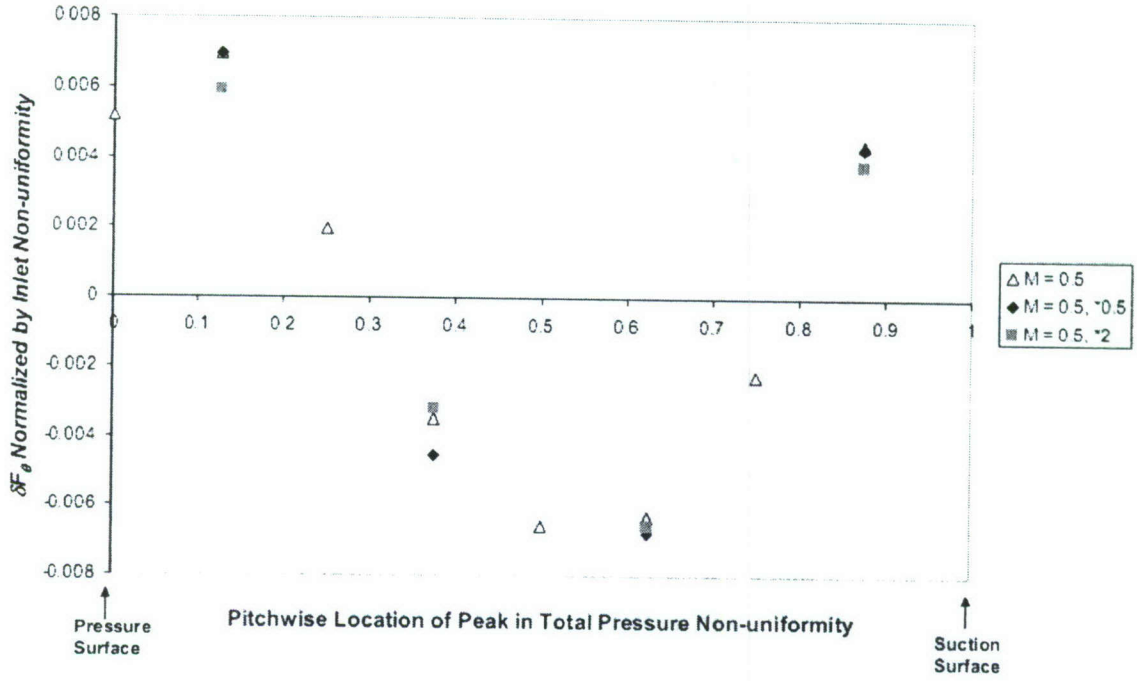

Figure 7.9: Non-dimensional force δF_θ normalized by the specified inlet total pressure non-uniformity as a function of the pitchwise position of total pressure non-uniformity δP_t; the magnitude of the inlet total pressure non-uniformity is varied while the inlet Mach number is held fixed (the first data set represents a nominal inlet non-uniformity magnitude; the second data set corresponds to when inlet non-uniformity is half the nominal value, and the third data set corresponds to when inlet non-uniformity is double the nominal value).

8.0 Estimating Rotor Performance Change in Three-dimensional Flow Situation

In this section we illustrate how one might use the flow model and the framework presented in Section 7 to provide an estimate of a change in rotor performance with blade-row spacing in a three-dimensional flow situation. Shown in Figure 8.1 is the computed (time-average) relative total pressure at two spanwise locations (one at 90% span in the tip region and the other at 46% span in the midspan region) for the far spacing configuration (see Section 4); the time-average trace of the IGV discrete wakes in the rotor passage varies from the hub to the tip region (in accordance with the variation in B3 parameter from the hub to the tip).

Now if we assume that at each spanwise location the flow is two-dimensional, then that at any given span, we can estimate the amplitude of the relative total pressure non-uniformity entering the rotor passage using Equation (7.3) and the phase of the wake (i.e., the pitchwise position of the relative total pressure non-uniformity distribution). The value of δF_θ can next be obtained using data such as that given in Figure 7.8 and 7.9. Thus an estimate of the spanwise distribution in δF_θ can be constructed. The estimated

spanwise distribution in δF_θ can be integrated along the span from hub to tip to give the net change in force, and hence work input, for the rotor.

The steps outlined above can be repeated for a change in the intra-blade row spacing (i.e. different value of B3 parameter). For the SMI geometry, the maximum possible change in tangential blade force associated with the resulting change in B3 parameter is estimated to 1.2% of the nominal blade force, which is not insignificant. The estimated change is in accord with the computed value from the unsteady three-dimensional flow simulations for the SMI stage for different IGV-rotor spacings.

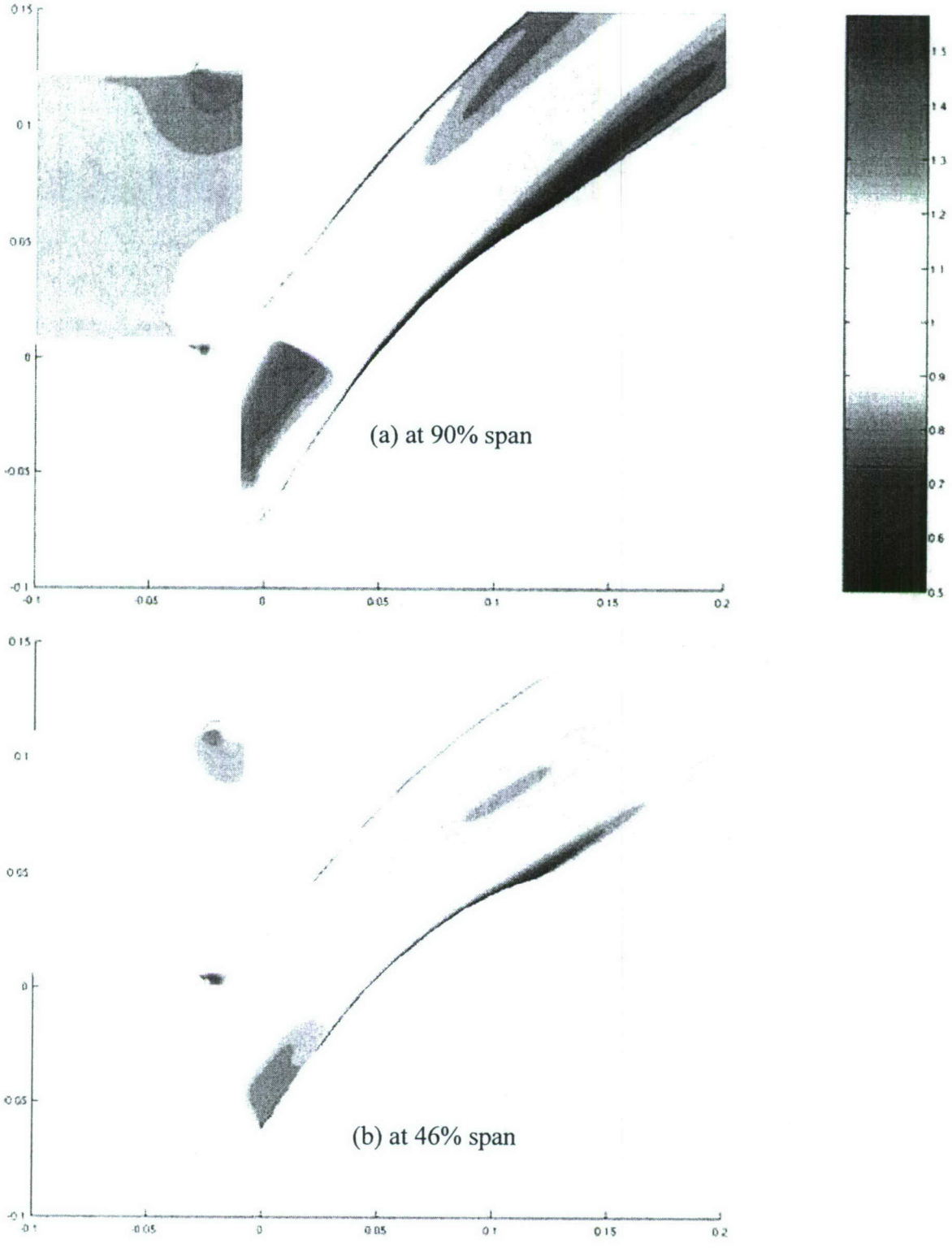

Figure 8.1: Computed time-average relative total pressure distribution at (a) 90% span (tip region and (b) 46% span (midspan region) for the far spacing SMI configuration.

9.0 Overall Summary and Conclusions

- The impact of axial blade row spacing on rotor performance for a highly-loaded, high Mach number single stage compressor has been assessed using time accurate, three-dimensional computations for two axial blade row spacings. At the same mass flow rate, the reduced spacing had a 0.7 point lower efficiency and a 1% lower work input than the larger spacing.

- A numerical technique was developed to accurately quantify entropy generation from computational simulations, even in regions with high spatial gradients, such as shock waves. The technique used the divergence of velocity as a marker to precisely define the shock region.

- The dominant entropy generating mechanism that leads to the performance differences between the configurations is associated with the vortices which are shed from the upstream vanes due to the rotor pressure field.

- The vortex trajectory within the rotor, which is a function of blade row spacing, impacts rotor performance. Two-dimensional computations were carried out for two axial blade row spacings with different vortex trajectories. In one configuration, one shed vortex was located within the boundary layer and one outside the boundary layer (in the core flow). In the other configuration, both vortices were located in the core flow. The latter configuration had a 3% lower work input and a 0.3 point difference in efficiency, as measured far downstream of the rotor.

- For a two-dimensional geometry at a given Mach number, the vortex trajectory is found to be a function of the ratio between the convective time scale for the vortices to travel the length of the axial gap between the vane and rotor blade rows, and the rotor period (i.e. the time for a rotor to move one rotor pitch).

- The largest difference in the entropy generation between the two configurations investigated occurred downstream of the rotor trailing edge. This is due to different mixing processes that result from differences in the rotor boundary layer and the different number of the vortices located in the core flow.

- The flow in a two-dimensional diffuser subjected to a wake and jet is used to provide a physical context explaining the response of the rotor performance to the discrete wakes.

- A steady-state flow model is developed for estimating the change in rotor performance with interblade row spacing.

- The scaling of the effect associated with IGV-rotor interactions is established in terms of inlet Mach number, flow (relative total pressure) non-uniformity associated with IGV discrete wakes, and the B3 parameter (which is the ratio between the convective

time scale for the vortices to travel the length of the axial gap between the vane and rotor blade rows, and the rotor period).

10.0 References

Beach, T., 2003. Personal communication with Gorrell, S.E., AP Solutions.

Chen, J.P., Briley, W. R., 2001, "A Parallel Flow Solver for Unsteady Multiple Blade Row Turbomachinery Simulations," ASME-2001-GT-0348.

Chen, J.P., Celestina M.L., and Adamczyk J.J., 1994. "A New Procedure for Simulating Unsteady Flows through Turbomachinery Blade Passage," *ASME Paper 94-GT-151.*

Chen J.P., and Barter, J.W., 1998. "Comparison of Time-Accurate Calculations for the Unsteady Interaction in Turbomachinery Stage," *AIAA-98-3292.*

Chriss, R.M., Copenhaver, W.W., and Gorrell, S.E., 1999. "The Effects of Blade-Row Spacing on the Flow Capacity of a Transonic Rotor," *ASME Paper 99-GT-209.*

Cumpsty, N.A., 1989, *Compressor Aerodynamics*, Longman Group UK Limited, London.

Denton, J.D., 1993, "Loss Mechanisms in Turbomachines - The 1993 IGTI Scholar Lecture," *ASME J. Turbomachinery*, Vol. 115, pp. 621-656.

Drela, M., Youngren, H., 1998, "A User's Guide to MISES 2.53," MIT Computational Aerospace Science Laboratory.

Erdos, J.I., Alzner, E., and McNally W., 1997. "Numerical Solution of Periodic Transonic Flow through a Fan Stage," *AIAA Journal,* **15**(11), pp. 1559-1568.

Gorrell, S.E., 2001. "An Experimental and Numerical Investigation of Stator-Rotor Interactions in a Transonic Compressor," Ph.D. Dissertation, Department of Mechanical Engineering, Iowa State University.

Gorrell, S.E., Okiishi, T.H., and Copenhaver, W.W., 2003. "Stator-Rotor Interactions in a Transonic Compressor, Part 1: Effect of Blade-Row Spacing on Performance," *ASME Journal of Turbomachinery,* **125**(2), pp. 328-335.

Gorrell, S.E., Okiishi, T.H., and Copenhaver, W.W., 2003. "Stator-Rotor Interactions in a Transonic Compressor, Part 2: Description of a Loss-Producing Mechanism," *ASME Journal of Turbomachinery,* **125**(2), pp. 336-345.

Gorrell, S.E., Car, D., Puterbaugh, S.L., Estevadeordal, J., and Okiishi, T.H., 2005. "An Investigation of Wake-Shock Interactions in a Transonic Compressor With Digital Particle Image Velocimetry and Time-Accurate Computational Fluid Dynamics," *ASME Journal of Turbomachinery,* **128**(4), pp. 616-626.

Gorrell, S.E., 2006, Personal communication, U.S. Air Force Research Laboratory, Wright Patterson Air Force Base, Ohio.

Greitzer, E.M., Tan, C.S., Graf, M.B., 2004, *Internal Flow: Concepts and Applications*, Cambridge University Press.

Hetherington, R., Moritz, R. R., 1977, "The Influence of Unsteady Flow Phenomena on the Design and Operation of Aero Engines", *Unsteady Phenomena in Turbomachinery*, AGARD CP-177, North Atlantic Treaty Organization.

Khalid, S. A., Khalsa, A. S., Waitz, I. A., Tan, C. S, Greitzer, E. M., Cumpsty, N. A., Adamczyk, J., Marble, F. E., 1999, "Endwall Blockage in Axial Compressors," *ASME Journal of Turbomachinery*, Vol. 121.

Koch C. C., 1981. Stalling pressure rise capability of axial flow compressor stages. *ASME J. of Engineering for Power*, 103: 645-56.

Mikolajczack, A. A., 1977, "The Practical Importance of Unsteady Flow", *Unsteady*

Phenomena in Turbomachinery, AGARD CP-144, North Atlantic Treaty Organization.

Morfey, C.L., and Fisher, M.J., 1970. "Shock-wave Radiation from a Supersonic Ducted Rotor," *Aeronautical Journal, Royal Aeronautical Society,* 74(715), pp. 579-585.

Shabbir, A., Adamczyk, J.J., 2004, "Flow Mechanism for Stall Margin Improvement Due To
Circumferential Casing Grooves On Axial Compressors," ASME-GT2004-53903.

Shum, Y.K., Tan, C. S., Cumpsty, N. A., 2000, "Impeller-Diffuser Interaction in Centrifugal Compressor," *ASME J. Turbomachinery*, Vol. 122, No. 4.

Smith L.H., 1970, "Casing Boundary Layers in Multistage Axial Flow Compressors", *Flow Research on Blading*, L.S. Dzung, ed., Elsevier Publishing Company.

Smith, L.H., 1993, "Wake Ingestion Propulsion Benefits", *J. Propulsion & Power*, Vol. 9, No. 1.

Sirakov, B., Tan, C. S., 2003, "Effect Of Unsteady Stator Wake – Rotor Double-Leakage Tip Clearance Flow Interaction On Time-Average Compressor Performance", ASME *J. of Turbomachinery*, Vol. 125, No. 3.

Turner, M.G., Gorrell, S.E., and Car, D., 2005. "Radial Migration of Shed Vortices in a Transonic Rotor Following a Wake Generator: A Comparison Between Time Accurate and Average Passage Approach," *ASME Paper GT2005-68776.*

Valkov, T., Tan, C.S., 1999, "Effects of Upstream Rotor Vortical Disturbances on Time-Average Performance of Axial Compressor Stator: Part 1- Framework of Technical Approach and Rotor Wakes-Stator Blade Interaction, and Part 2- Rotor Tip Leakage and Discrete Streamwise Vortex -Stator Blade Interaction" *ASME J. Turbomachinery,* Vol. 121, No. 3.

Villanueva, A.V., 2006. "Characterization of the Flow Field Response to Vaneless Space Reduction in Centrifugal Compressors," M.Sc. Thesis, Department of Aeronautics and Astronautics, Massachusetts Institute of Technology.

Wang, X.,and Chen, J.P., 2004. "A Post-Processor to Render Turbomachinery Flows Using Phase-Lag Simulations," *AIAA-2004-615, 42nd AIAA Aerospace Sciences Meeting and Exhibit*, pp. 5997-6003.

Wisler, D.C., 1998, "Axial –Flow Compressor and Fan Aerodynamics" *in Handbook of Fluid Dynamics*, R. W. Johnson, ed., CRC Press, Boca Raton, FL

Zachial, A. and Nurnberger, D., 2003. "A Numerical Study on the Influence of Vane-Blade Spacing on a Compressor Stage at Sub- and Transonic Operating Conditions," *ASME Paper GT2003-38020*

11.0 Appendices

Appendix A
Non-uniformity Metric

In Section (6.3), a metric to measure the degree of non-uniformity ahead of the rotor was defined as:

$$\frac{1}{2}\rho u'^2, \tag{6.6}$$

where u'^2 is a perturbation velocity, defined as:

$$u'^2 = (u_x - \bar{u}_x)^2 + (u_y - \bar{u}_y)^2. \tag{6.7}$$

The overbar represents the time- and pitch-wise area- average of the velocity component. The non-uniformity metric is averaged over the pitch and in time, and non-dimensionalized by the dynamic head at the inlet. Its mathematical form is:

$$\frac{\overline{\frac{1}{2}\rho u'^2}}{p_{t,inlet} - p_{inlet}} = \frac{\frac{1}{\tau}\frac{1}{A_{total}}\int\left[\int\frac{1}{2}\rho u'^2 dA\right]dt}{p_{t,inlet} - p_{inlet}}. \tag{6.8}$$

The averaged quantity in (6.8) will now be shown to be a suitable metric to define the non-uniformity in the flow field. This is first shown by demonstrating that the non-uniformity metric represents the pressure difference between two axial planes by using the conservation of momentum (however, the factor of ½ does not appear). Using linear momentum, the non-uniformity in the flow field can be shown to act as a blockage that decreases the flow area, and hence, reduces the pressure. The non-uniformity can also be related to the stagnation pressure losses if the flow at an axial location was allowed to mix to a uniform state.

First, linear momentum is used to determine how non-uniformity affects pressure changes in a flow. The impulse function is written as:

$$I = p + \rho u^2. \tag{A.1}$$

The impulse function, when integrated across the inlet and exit flow area (planes 'a' and 'b') of a specified control volume, is the same if there are no forces acting on the control volume and there is no change in area. Steady flow is assumed. Mathematically, this is stated as:

$$\overline{\Delta I} = \overline{I_b} - \overline{I_a} = 0 \tag{A.2}$$

The overbar in this equation, and in the rest of this section, represents the pitch-wise or area-average of the impulse function. Pressure and velocity at any point can be defined as the sum of its average quantity on the plane of interest, plus its spatially-varying quantity:

$$p = \overline{p} + p' \tag{A.3}$$

$$u = \overline{u} + u' \tag{A.4}$$

Note that the area-average of the spatially-varying component of the pressure and velocity are zero, i.e. $\overline{p'} = 0$ and $\overline{u'} = 0$.

Substituting the expressions of A.3 and A.4 into the impulse function:

$$I = \overline{p} + p' + \rho\left(\overline{u}^2 + 2\overline{u}u' + u'^2\right) \tag{A.5}$$

By assuming the density and cross-sectional area remains constant, the continuity equation simplifies to: $\overline{u_a} = \overline{u_b}$. The difference in the momentum between planes 'a' and 'b' is:

$$\Delta I = \overline{p}_b - \overline{p}_a + p'_b - p'_a + 2\overline{u}\rho\left(u'_b - u'_a\right) + \rho\left(u'^2_b - u'^2_a\right) \tag{A.6}$$

Area-averaging the impulse function gives:

$$\overline{\Delta I} = \overline{p}_b - \overline{p}_a + \rho\left(\overline{u'^2_b} - \overline{u'^2_a}\right) = 0 \tag{A.7}$$

The difference in pressure from planes 'a' to 'b' is therefore related to the non-uniformity at both stations by rearranging (A.7):

$$\overline{p}_b - \overline{p}_a = -\rho\left(\overline{u'^2_b} - \overline{u'^2_a}\right) = -\rho\Delta\overline{u'^2} \tag{A.8}$$

If at plane 'b', the flow is fully mixed out, then:

$$\overline{p}_b - \overline{p}_a = \rho\overline{u'^2_a} \tag{A.9}$$

The term on the right-hand side of A.9 is similar to the non-uniformity metric, and therefore indicates that the metric represents the pressure rise that would be obtained if the non-uniformity was allowed to mix to a uniform state. Therefore, the non-uniformity represents a blockage in the flow area, which tends to reduce pressure.
The ½ term included in the non-uniformity metric appears when considering the difference in mass-averaged stagnation pressure differences between planes 'a' and 'b'. The stagnation pressure for incompressible flow is given as:

$$p_t = p + \frac{1}{2}\rho u^2 \tag{A.10}$$

The stagnation pressure can be multiplied by the velocity and averaged across the pitch to find a velocity-weighted average value for the stagnation pressure. This is equivalent to multiplying the stagnation pressure by the local mass flux and finding a mass-averaged stagnation pressure. However, the density is not included when multiplying by the mass flux because the density is assumed constant, and therefore is not required when comparing two axial locations. The velocity-weighted stagnation pressure is written as:

$$up_t = up + \frac{1}{2}\rho u^3 \tag{A.11}$$

Substituting the expressions for pressure and velocity from (A.3) and (A.4) into (A.11):

$$up_t = \overline{u}\overline{p} + \overline{u}p' + + u'\overline{p} + u'p' + \frac{1}{2}\rho\left(\overline{u}^3 + 3\overline{u}^2 u' + 3\overline{u}u'^2 + u'^3\right) \tag{A.12}$$

A pitch-wise average of (A.12) gives:

$$\overline{up_t} = \overline{up} + \overline{u'p'} + \frac{1}{2}\rho\overline{u}^3 + \frac{3}{2}\rho\overline{u}\,\overline{u'^2} + \frac{1}{2}\rho\overline{u'^3} \tag{A.13}$$

The difference in mass-averaged stagnation pressure between planes 'a' and 'b' becomes (by also applying the continuity equation):

$$\Delta\overline{up_t} = \overline{u}\Delta\overline{p} + \Delta\overline{u'p'} + \frac{3}{2}\rho\overline{u}\Delta\overline{u'^2} + \frac{1}{2}\rho\Delta\overline{u'^3} \tag{A.14}$$

Using the pressure difference from conservation of linear momentum given in (A.8), the first term on the left-hand side of (A.14) can be replaced:

$$\Delta\overline{up_t} = \overline{u}\left(-\rho\Delta\overline{u'^2}\right) + \Delta\overline{u'p'} + \frac{3}{2}\rho\overline{u}\Delta\overline{u'^2} + \frac{1}{2}\rho\Delta\overline{u'^3} \tag{A.15}$$

which reduces to:

$$\Delta\overline{up_t} = \Delta\overline{u'p'} + \frac{1}{2}\rho\overline{u}\Delta\overline{u'^2} + \frac{1}{2}\rho\Delta\overline{u'^3} \tag{A.16}$$

For a non-uniform flow that does not have large variations in the velocity profile, the approximation $\overline{u}\Delta\overline{u'^2} >> \Delta\overline{u'^3}$ is valid. Furthermore, for one-dimensional shear flow, $p' = 0$. The expression in (A.15) becomes:

$$\Delta\overline{up_t} = \overline{u}\left(\frac{1}{2}\rho\Delta\overline{u'^2}\right) \tag{A.17}$$

Therefore, the non-uniformity metric at any plane represents the potential for stagnation pressure losses if the flow at that axial location was allowed to mix to a uniform state in a constant area duct. The assumptions include incompressible, one-dimensional flow, which makes the use of the non-uniformity metric approximate.

Finally, the non-uniformity metric also represents the difference between the area-averaged stagnation pressure and the stagnation pressure based on the average quantities on an axial plane. The latter stagnation pressure is given as:

$$\hat{p}_t = \overline{p} + \frac{1}{2}\rho\overline{u}^2 \tag{A.18}$$

An area-average of the stagnation pressure $\overline{p}_t^A$ is (since area-average of u' and p' are zero):

$$\overline{p}_t^A = \overline{p} + \frac{1}{2}\rho\left(\overline{u}^2 + \overline{u'^2}\right) \tag{A.19}$$

And the difference between (A.18) and (A.19) also leads to the expression of the non-uniformity metric:

$$\overline{p}_t^A - \hat{p}_t = \frac{1}{2}\rho\overline{u'^2} \tag{A.20}$$

In summary, the non-uniformity metric calculated in (6.8) at any axial plane of interest represents a number of physical quantities: the blockage at that location, the potential for stagnation pressure losses, and the difference in the area-averaged stagnation pressure compared to the stagnation pressure compared from the average values of pressure and velocity at that location. All three physical scenarios are an indication of the level of non-uniformity at a specified location.

The analysis of the present section assumed that the flow non-uniformity was constant in time. However, since the flow field at any axial location is unsteady, the non-uniformity metric is adjusted by computing the perturbation velocity given in (6.7) with respect to the time- and pitch-wise average of the velocity component. This makes the non-uniformity metric an approximation, but nonetheless provides a suitable quantity when comparing similar flow fields for the two configurations that were discussed in Section 6.

Appendix B
Mixing of Boundary Layers to a Uniform Flow State

In Section 6, two-dimensional calculations were conducted to study the effect of a change in vortex trajectory on rotor performance. Two configurations under examination were referred to as "far$_{2D}$" and "close$_{2D}$." At the rotor trailing edge plane, the boundary layer characteristic quantities are measured from expressions given in Equation (6.9)-(6.11) for both configurations. The present discussion outlines the procedure to determine the contribution of the boundary layers to the entropy rise from the rotor trailing edge plane to far downstream, where the flow field is uniform.

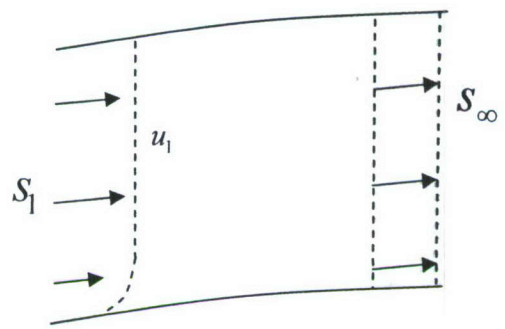

Figure B.1: Schematic that represents the mixing of a swirling flow to a uniform flow state.

To determine the entropy rise from the boundary layers alone, the first assumption is that the core flow is uniform in the pitch-wise direction, as seen in Figure B.1. Then the conservation equations are applied from the rotor trailing edge plane to far downstream, allowing the boundary layers to mix with the core flow to a uniform flow state. The conservation equations include conservation of mass, linear and angular momentum, and energy. A swirl angle is also measured at the rotor exit and included in the mixing calculations to better represent the flow field. Other required quantities to define the rotor exit state of are the time-averaged mass flow rate, as well as the mass- and time-averaged pressure, and entropy flux. The temperature and density are found from the constitutive relation for entropy.

A control volume is placed from the rotor exit to far downstream. The conservation equations are:

$$\dot{m} = \rho u_1 \left(A - \delta^*\right)\cos\alpha_1 = \rho u_\infty A \cos\alpha_\infty \tag{B.1}$$

$$p_1 A + \rho u_1^2 \cos^2\alpha_1 \left(A - \theta - \delta^*\right) = p_\infty A + \rho u_\infty^2 \cos^2\alpha_\infty A \tag{B.2}$$

$$\rho u_1^2 \sin\alpha_1 \cos\alpha_1 \left(A - \theta - \delta^*\right) = \rho u_\infty^2 \sin\alpha_\infty \cos\alpha_\infty A \tag{B.3}$$

$$c_p T_1 \dot{m} + \frac{\rho u_1^3}{2} \cos\alpha_1 \left(A - \delta^* - \theta^*\right) = \left(c_p T_\infty + \frac{u_\infty^2}{2}\right)\dot{m} \tag{B.4}$$

The ideal gas law is also used:

$$p = \rho R T \tag{B.5}$$

The constitutive relation to calculate the entropy rise is:

$$\Delta s / R = \frac{\gamma}{\gamma - 1} \ln\left(\frac{T_{t_\infty}}{T_{t_1}}\right) - \ln\left(\frac{p_{t_\infty}}{p_{t_1}}\right) \tag{B.6}$$

From mass conservation in (B.1), the uniform core velocity, u_1, can be found since the mass flow rate is measured, and all other quantities are known. The values at downstream infinity can then be determined by solving Equation (B.1)-(B.5) simultaneously, and the entropy rise calculated from Equation (B.6).

The entropy increase from the rotor leading edge to downstream infinity was independent of the value of the entropy flux at the rotor leading edge. There was a slight dependence of the entropy rise due to mixing on pressure. Varying the pressure at the rotor exit by 1.3% (which is the difference between the mass-averaged and area-averaged pressure) caused the difference in entropy rise between the two configurations to change by 2.5%. This difference in the entropy rise was not enough to change the conclusions derived from the mixing calculation. The results of the mixing calculations are presented in Table 6.7.

12.0 Personnel Supported

C. S. Tan	Senior Research Engineer
E. M. Greitzer	Slater Professor of Aeronautics and Astronautics
Sean Nolan	Graduate Student (PhD student)
Barbara Botros	Graduate Student (MS student)
M. Jenkins	Graduate Student (MS Student)
H. Anderson	Fiscal Officer
J. Finn	Administrative Assistant

13.0 Publications

Vo, H., Tan, C. S., Greitzer, E. M., 2008, " Criteria for Spike Initiated Rotating Stall", *ASME J. of Turbomachinery*, Vol. 130, No. 1.
From research supported under previous AFOSR GRANT F49620-00-1-0014

14.0 Theses

Nolan, S., "Effect of Radial Transport on Compressor Tip Flow Structures and Enhancement of Stable Flow Range", MS Thesis, Department of Aeronautics and Astronautics, Massachusetts Institute of Technology, June 2005.[7]

B. Botros, "Impact of Unsteady Flow Processes on the Performance of a High Speed Axial Flow Compressor", SM Thesis, MIT Department of Mechanical Engineering, February, 2008.

S. Nolan, "Modeling and Scaling of Unsteady Blade-rows Interaction Effects in Hist-Stage Loading High Mach Number compressors", PhD Thesis, MIT Department of Aeronautics and Astronautics, expected September, 2008.

15.0 Honors and Awards

ASME Tom Sawyer Award to E. M. Greitzer at the 2005 ASME International Gas Turbine Conference in Reno, Nevada.

2007 IGTI Scholar Lecture Award to E. M. Greitzer on " 'Some Aerodynamic Problems of Aircraft Engines' – Fifty Years After"

16.0 Transitions

None

---

[7] Also partially supported by U.S. Air Force Contract #F33615-02-D-2223, Dr. Rabe the technical monitor at AFRL Wright Field

17.0 AFRL Points of Contact

Dr. Steve Puterbaugh, (937) 255-7432 (email: steven.puterbaugh@wpafb.af.mil), Dr. S. Gorrell and Mr. D. Car, who also participate in bi-weekly research meetings.
Dr. D. Rabe, (937) 255-6802 x231 (email: Douglas.Rabe@wpafb.af.mil)
Dr. John Adamczyk, retired scientist from NASA GRC, has also contributed much to the research

18.0 AFRL-MIT Collaboration

At the encouragement of AFOSR Program Managers, the MIT Gas Turbine Laboratory and the Compressor Aerodynamic Research Laboratory (CARL) of AFRL have been collaborating in research supported under AFOSR GRANT FA9550-05-1-0050. The collaboration consists of: (i) regular semi-weekly teleconference which includes sharing of ideas and interpretation of computed results as well as useful suggestions on the research; (ii) AFRL providing computational resources and experimental information; and (iii) a member of the CARL research team (Dr. S. Gorrell) serving on the Doctoral Thesis Committee of Sean Nolan.

On November 27, a discussion of the research results of this collaboration was held at AFRL. The participants were S. Puterbaugh (AFRL), S. Gorrell (AFRL), D. Car (AFRL), T. Bailie (AFRL), S. Nolan (MIT), E. M. Greitzer (MIT) and C. S. Tan (MIT). There was an initial presentation by Mr. S. Nolan, a graduate student involved in the project, followed by technical discussions. Most of the discussion focused on a new mechanism that had been identified and quantified for its impact on the performance of high-stage loading high-Mach number (HLHM) compressors.

Discussion was also undertaken to scope out the technical content for a proposed joint AFRL-MIT paper. The main aspects examined were what additional research tasks are needed to produce a high quality paper that clearly describes, and quantifies, this new mechanism.

In addition Sean Nolan (the doctoral student supported under AFOSR Grant) will be at the AFRL as a PhD co-op from January to August 2008 to further his doctoral research. While at AFRL he will be under the joint supervision of Dr. S. Puterbaugh of CARL and Dr. D. Rabe of CRF. During this period, we will again have semi-weekly teleconferences to discuss the research progress.

The research team at CARL (see above for the list) and at the MIT Gas Turbine Laboratory view the collaboration as highly successful in terms not only of working relationships, but also the scientific output produced.